Spatial and Temporal Variability of the M_2 Internal Tide Generation and Propagation on the Oregon Shelf

J. J. OSBORNE, A. L. KURAPOV, G. D. EGBERT, AND P. M. KOSRO

College of Oceanic and Atmospheric Sciences, Oregon State University, Corvallis, Oregon

ABSTRACT

A 1-km-horizontal-resolution model based on the Regional Ocean Modeling System is implemented along the Oregon coast to study average characteristics and intermittency of the M_2 internal tide during summer upwelling. Wind-driven and tidally driven flows are simulated in combination, using realistic bathymetry, atmospheric forcing, and boundary conditions. The study period is April through August 2002, when mooring velocities are available for comparison. Modeled subtidal and tidal variability on the shelf are in good quantitative agreement with moored velocity time series observations. Depth-integrated baroclinic tidal energy flux (**EF**), its divergence, and topographic energy conversion (TEC) from the barotropic to baroclinic tide are computed from high-pass-filtered, harmonically analyzed model results in a series of 16-day time windows. Model results reveal several "hot spots" of intensive TEC on the slope. At these locations, TEC is well balanced by **EF** divergence. Changes in background stratification and currents associated with wind-driven upwelling and downwelling do not appreciably affect TEC hot spot locations but may affect intensity of internal tide generation at those locations. Relatively little internal tide is generated on the shelf. Areas of supercritical slope near the shelf break partially reflect baroclinic tidal energy to deeper water, contributing to spatial variability in seasonally averaged on-shelf **EF**. Despite significant temporal and spatial variability in the internal tide, the alongshore-integrated flux of internal tide energy onto the Oregon shelf, where it is dissipated, does not vary much with time. Approximately 65% of the M_2 baroclinic tidal energy generated on the slope is dissipated there, and the rest is radiated toward the shelf and interior ocean in roughly equal proportions. An experiment with smoother bathymetry reveals that slope-integrated TEC is more sensitive to bathymetric roughness than on-shelf **EF**.

1. Introduction

In summer, currents over the Oregon shelf (U.S. West Coast) are predominantly wind driven, varying on the temporal scale of several days. The wind-driven along-shore current is predominantly to the south, vertically sheared, and associated with upwelling of cold waters near the coast (Allen et al. 1995). At the surface, summer-average magnitude of the wind-driven jet is near 0.5 m s^{-1}. Tides are relatively moderate. The dominant barotropic tidal constituent off Oregon is M_2. Although the M_2 tidal depth-averaged currents are rather small, less than 0.05 m s^{-1} (Erofeeva et al. 2003), they flow over variable bathymetry and generate baroclinic motions near the M_2 tidal period (12.4 h; Baines 1982), resulting in an

internal tide that can be 0.1–0.15 m s^{-1}, based on mooring observations (Hayes and Halpern 1976; Torgrimson and Hickey 1979; Erofeeva et al. 2003). The internal tide thus can be an important contributor to current variability at the surface. Near the bottom, where the wind-driven current is weaker, internal tide currents can potentially dominate.

The characteristic horizontal length scale of the M_2 internal tide over the shelf is $O(10 \text{ km})$. Internal tide generation and propagation are sensitive to variability in background currents and hydrographic conditions associated with wind-driven upwelling and mesoscale eddies (Mooers 1970, 1975b,a; Chavanne et al. 2010; Chen et al. 2003; Park and Watts 2006; Pereira et al. 2007; Hall and Davies 2007; Xing and Davies 1997, 1998, 2005; for a brief review, see Kurapov et al. 2010). In particular, Xing and Davies (1997), using an idealized model, demonstrated that background changes associated with up-welling can increase the transfer of tidal energy to higher harmonics. Xing and Davies (2005) showed that a cold

Corresponding author address: John Osborne, COAS, Oregon State University, 104 COAS Admin. Bldg., Corvallis, OR 97331–5503.
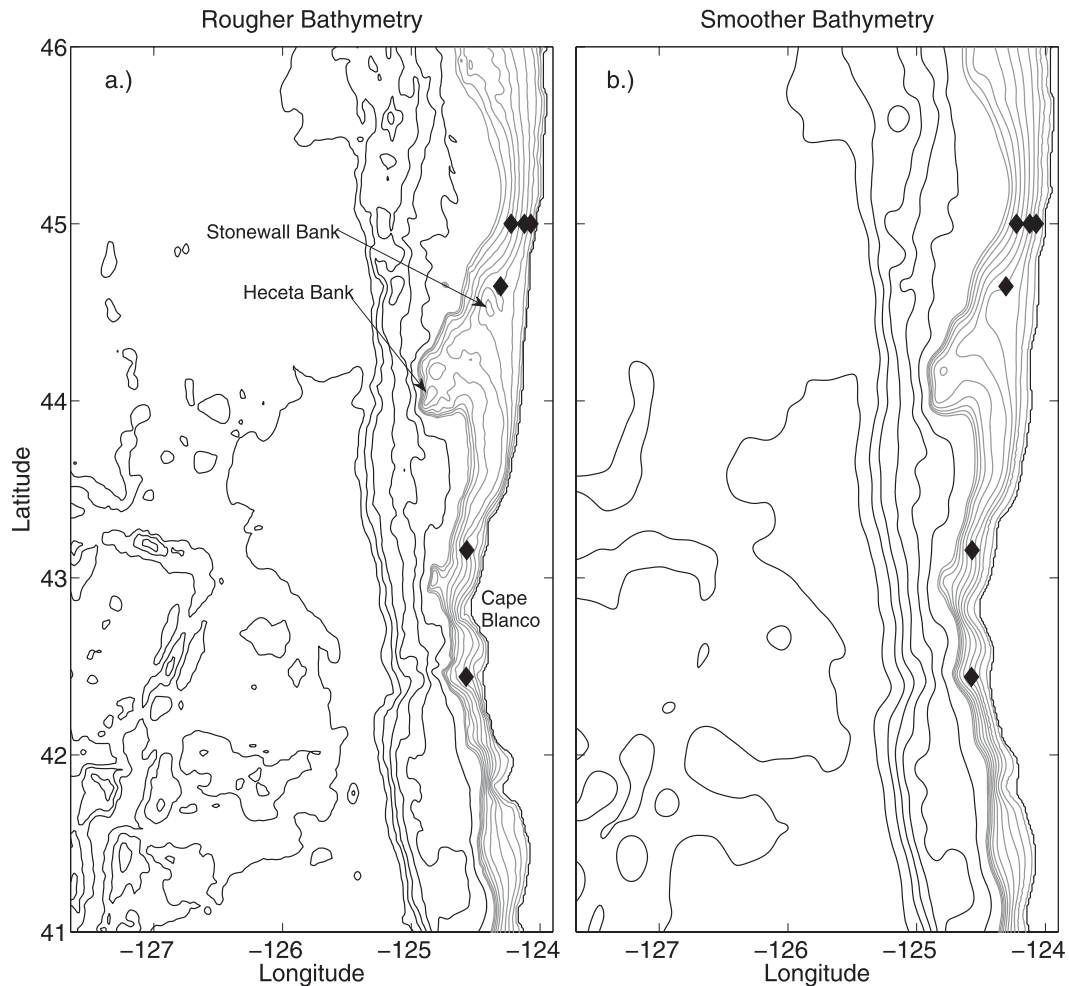E-mail: josborne@coas.oregonstate.edu

FIG. 1. Model domain and bathymetry. The black diamond symbols along 45°N show the location of three 2001 COAST ADCP moorings; the other diamonds are summer 2002 ADCP moorings. Half-tone contours are every 20 m, from the coast to 200-m depth; black contours are at every 500 m. (a) The rougher bathymetry case and (b) the smoother bathymetry case.

water dome can trap energy of propagating internal waves. Observations available in the coastal area are generally too sparse to resolve the resulting spatial and temporal intermittency of the internal tide. To describe this variability, provide estimates of the M_2 tidal energetics on the slope and shelf, and ultimately understand how the wind-driven and tidal flows influence each other, high-resolution model simulations seem to be the most promising approach.

In modeling studies off Oregon, wind-driven currents and internal tides have traditionally been studied separately (e.g., Kurapov et al. 2003; Allen et al. 1995; Federiuk and Allen 1995; Kurapov et al. 2005; Oke et al. 2002a,b; Springer et al. 2009; Koch et al. 2010). Recently, Kurapov et al. (2010) used the hydrostatic Regional Ocean Modeling System (ROMS; http://www.myroms.org)

to study influences of the wind-driven upwelling and internal tide in an idealized, two-dimensional (2D; cross-shore and vertical coordinates) setup. They found that internal tides with magnitudes comparable to those measured off Oregon affect subtidal cross-shore and alongshore transports. The utility of this 2D approach is limited, however, because the M_2 internal tidal motions are superinertial and freely propagate in three dimensions. Besides, the 2D approach may provide a misleading picture, because internal tides in such a model are only generated by the cross-shore barotropic tidal current flowing up and down the continental slope. In fact, off Oregon and in many other coastal environments, the M_2 barotropic tide propagates as a shelf-modified Kelvin wave, in which the M_2 tidal current is strongly polarized and aligned with the continental slope
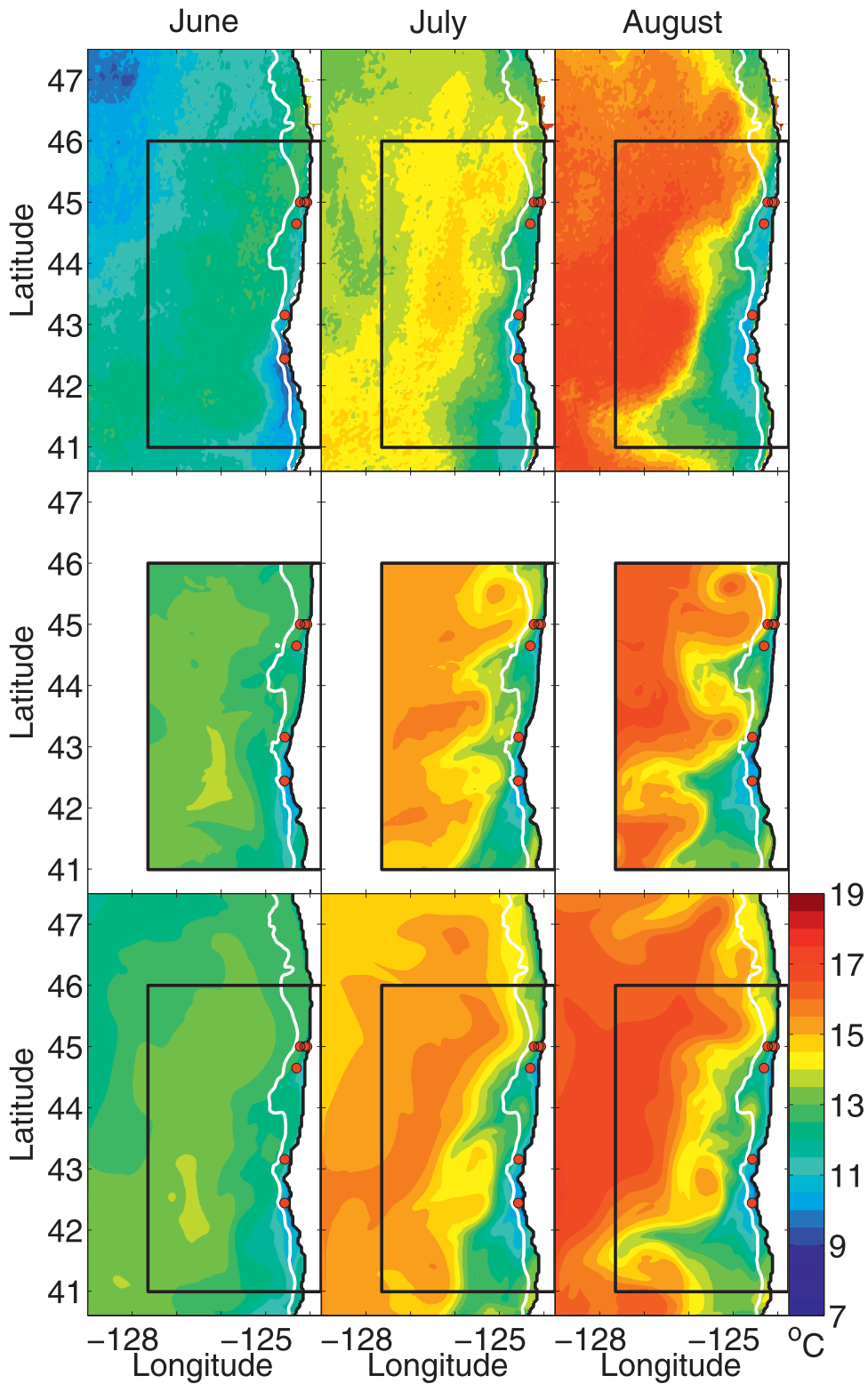
FIG. 2. Monthly averaged SST: (top) GOES (5.5-km resolution) satellite observations, (middle) the 1-km-resolution ROMS model, and (bottom) the 3-km resolution ROMS model that provided subtidal boundary conditions. Locations of ADCP moorings analyzed in this study are shown as red circles. The black rectangle is the domain of the 1-km model. The white contour is the 200-m isobath.
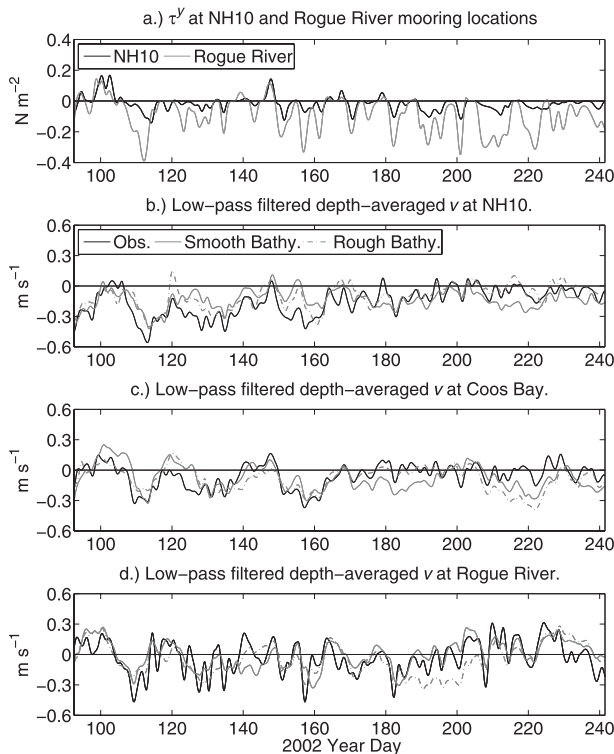
FIG. 3. (a) Meridional wind stress at the NH10 and Rogue River mooring locations. (b)–(d) 40-h low-pass-filtered, depth-averaged observed and model meridional velocities at the NH10, CB, and RR mooring locations, respectively.

bathymetry. Alongshore small-scale bathymetric variations can thus be important for internal tide generation, potentially resulting in an internal tide of greatly varying intensity along the coast.

In this paper, we analyze the output of a 3D model (described in section 2) that realistically represents both wind-driven and M_2 tidal flows over the Oregon shelf and slope (as verified against observations in section 3). We demonstrate strong nonuniformity of the M_2 internal tide generation along the Oregon slope and describe its intermittency (section 4). Some effects of bathymetry on model estimates of internal tide generation and on-shelf propagation are discussed in section 5. Section 6 provides a summary.

2. Model description

We use ROMS, a free-surface, hydrostatic, Boussinesq, terrain-following primitive-equation model featuring advanced numerics (Shchepetkin and McWilliams 2005). The model domain is approximately 300 km × 540 km (Fig. 1). The study period is 1 April through 31 August 2002. A thoroughly verified model solution of subtidal circulation off Oregon is available during the same period of time (Koch et al. 2010). It provides boundary conditions for our higher-resolution study. Data from the Global Ocean Ecosystem Dynamics (GLOBEC) field study (Batchelder et al. 2002) are available during this period, including mooring velocity profile measurements on the shelf. Note that internal tides on the Oregon shelf are generally stronger during summer than winter (Erofeeva et al. 2003) because the winter waters are well mixed because of seasonal downwelling and storms.

The model horizontal resolution is approximately 1 km. A total of 40 terrain-following s layers are used in the vertical, with an emphasis on resolving the surface and bottom boundary layers (using ROMS terminology, $\theta_s = 5$, $\theta_b = 0.4$, and thermocline = 50 m). Subgrid-scale turbulence is handled using the Mellor–Yamada 2.5 scheme (Mellor and Yamada 1982) modified by Galperin et al. (1988). The horizontal eddy diffusion and viscosity coefficients are set to 2 m^2 s^{-1} in the interior and increase over a 40-km sponge layer (via a sinusoidal ramp) to 15 m^2 s^{-1} at the three open boundaries. Bathymetry is a combination of the 5-minute gridded elevations/bathymetry for the world (ETOPO5; NOAA 1988) and the higher-resolution 12″ National Oceanic and Atmospheric Administration (NOAA)–National Geophysical Data Center bathymetry datasets. To investigate the effects of bathymetric resolution on internal tide energetics, cases using different degrees of bathymetric smoothing (Figs. 1a,b) have been considered. Smoothing is performed solving a pseudoheat equation with fixed values along the boundaries to preserve the shape of the coastline (Bennett 1992, chapter 2). The minimum depth is set to 10 m along the coast. Unless specifically mentioned, results for the case with rougher bathymetry are presented.

TABLE 1. Model–data statistics for the depth-averaged currents at mooring locations.

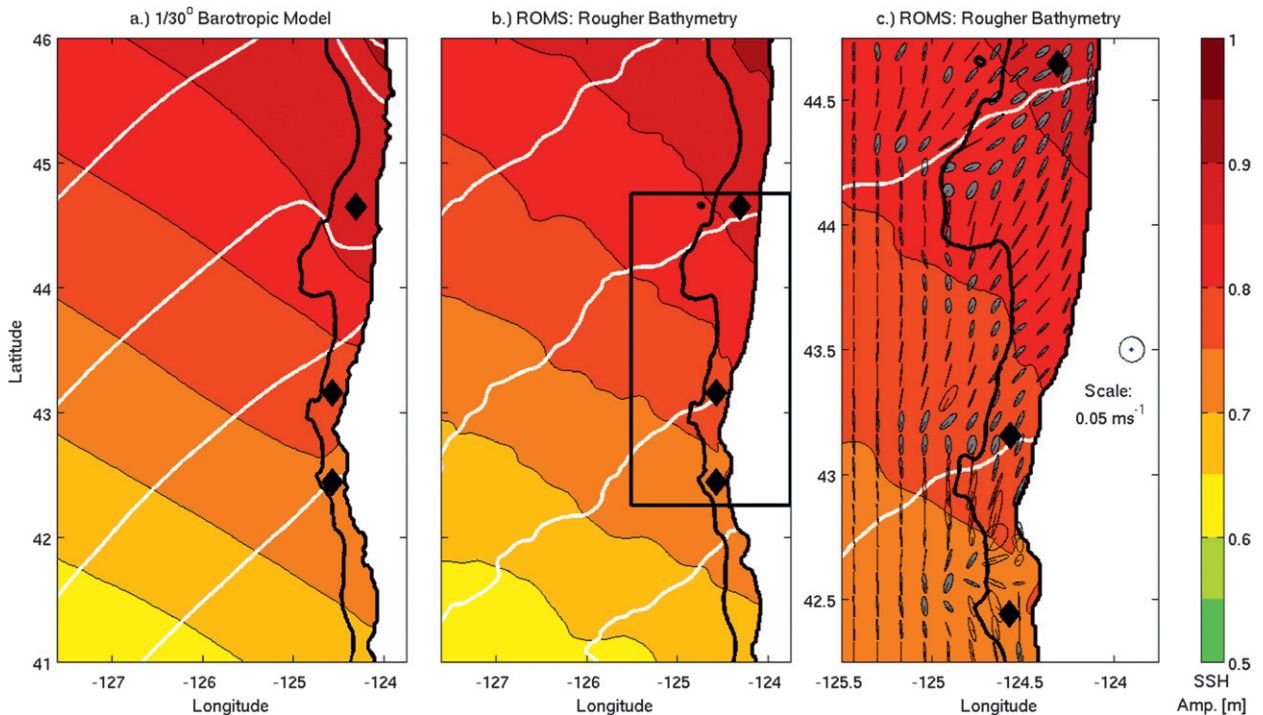| Statistic	Obs			Smoother bathymetry			Detailed bathymetry		
	NH10	CB	RR	NH10	CB	RR	NH10	CB	RR
Mean (m s^{-1})	−0.16	−0.06	−0.03	−0.14	−0.08	0.00	−0.11	−0.09	−0.05
Std dev (m s^{-1})	0.14	0.12	0.16	0.09	0.13	0.13	0.12	0.12	0.15
RMS (m s^{-1})	—	—	—	0.12	0.12	0.12	0.09	0.11	0.14
Complex correlation	—	—	—	0.44	0.48	0.64	0.72	0.47	0.59
Complex phase angle	—	—	—	3°	−1°	16°	1°	−3°	11°

FIG. 4. Barotropic M_2 sea surface elevation tidal amplitude and phase: (a) $1/30°$ shallow-water-equation model (Egbert et al. 1994; Egbert and Erofeeva 2002) providing tidal boundary conditions for our 1-km ROMS solution; (b) 1-km ROMS for the entire domain; and (c) 1-km ROMS for the close-up on the area shown as the black rectangle in (b), with horizontal barotropic tidal current ellipses added. Shaded (clear) ellipses indicate counterclockwise (clockwise) rotation. Black diamonds mark the NH10, CB, and RR moorings. White phase lines are 5° apart.

Subtidal boundary values (free-surface elevation, velocities, temperature, and salinity) are obtained by interpolation between snapshots from a larger-scale, 3-km-horizontal-resolution ROMS simulation forced by winds and heat fluxes but not tides (Koch et al. 2010). These boundary fields are provided every 48 h. Initial conditions are obtained from the same model. Flather (1976) and Chapman (1985) boundary conditions are used for normal barotropic velocities and the free surface, respectively. Passive/active radiation boundary conditions are applied for baroclinic velocities, temperature, and salinity (Marchesiello et al. 2001). Tidal forcing is added to the subtidal boundary conditions every time step using M_2 harmonic constant estimates of sea surface elevation amplitude and depth-averaged currents from a data-assimilating $1/30°$-resolution barotropic tidal model (Egbert et al. 1994; Egbert and Erofeeva 2002). Although this adds barotropic tides to the boundary (which then propagate into the domain), data for internal tides at the boundary are unavailable and their omission is a potential source of error. To simplify analysis, only the dominant M_2 tidal constituent is included in tidal forcing.

Atmospheric momentum and heat flux are computed using the bulk flux formulation adapted in ROMS (Fairall et al. 1996a,b). The daily averaged wind speed is obtained from the Coupled Ocean–Atmosphere Mesoscale Prediction System (COAMPS; Hodur 1997) and inputs for heat flux computations (air temperature and pressure, relative humidity, and solar shortwave radiation; all monthly averaged) from the National Centers for Environmental Prediction (NCEP) reanalysis (Kalnay et al. 1996). The meridional wind stress is well correlated along the Oregon coast: for example, as can be seen in the time series at two midshelf locations near 44.7° and 42.4°N [near the NH10 and Rogue River (RR) moorings, described below; Fig. 3a]. The wind stress is substantially stronger south of Cape Blanco (42.8°N) because of orographic effects (Samelson et al. 2002).

3. Model verification

We first verify the accuracy of the subinertial wind-driven circulation and the tidally forced flows. To separate subinertial (mostly wind driven) and superinertial (mostly tidal) variability for this analysis, a 40-h half-amplitude low-pass filter is applied to both
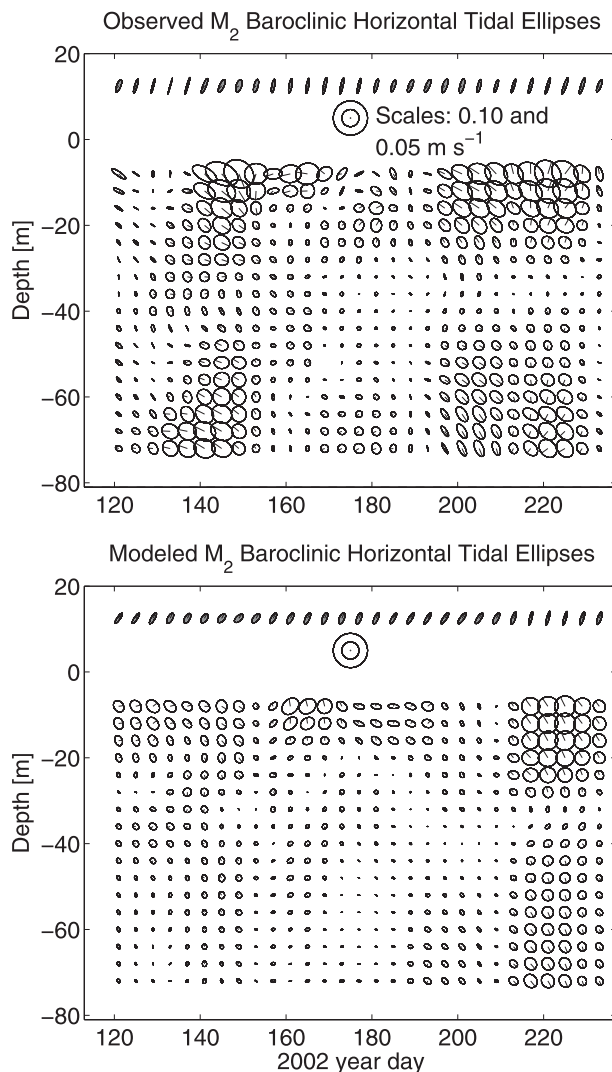
FIG. 5. (top) Observed and (bottom) modeled barotropic and baroclinic tidal ellipses at NH10 ($h = 81$ m). The vertical axis represents the depth of each tidal ellipse and the horizontal axis time (center of each 16-day analysis window). Ellipses above 10-m depth correspond to barotropic tides. Northward velocity is directed up and eastward velocity is directed to the right. Shaded (unshaded) ellipses indicate counterclockwise (clockwise) rotation.

observed and modeled time series. To describe tidal intermittency, high-pass-filtered time series are harmonically analyzed in a series of relatively short overlapping time windows. In each window, the high-pass-filtered signal is assumed to be harmonic: for example, $u(x, y, z, t) = \mathrm{Re}[\tilde{u}(x, y, z)e^{i\omega t}]$, where ω is the M_2 angular frequency (1.405×10^{-3} rad s^{-1}) and $\tilde{u}$ is a complex harmonic constant. In our case, the windows are chosen to be 16 days long to allow separation of the M_2 and S_2 tidal constituents in the data and thus facilitate

model–data comparisons. Also, for the purposes of this study, we define barotropic current as depth-averaged current and baroclinic current as the deviation from the depth average. Note that separation of the flow into barotropic and baroclinic components over varying bathymetry is not trivial. For instance, the bottom boundary layer would introduce vertical variability in barotropic tidal flows. Variability in the bottom boundary layer associated with wind-driven processes can introduce some intermittency in estimates of barotropic (depth averaged) tidal currents. The definition adopted here allows clear separation of equations for the barotropic and baroclinic tidal energy but is not without shortcomings (for further details, see Kurapov et al. 2003).

a. Wind-driven circulation

Maps of monthly averaged SST from the 5.5-km-resolution Geostationary Operational Environmental Satellite (GOES; Maturi et al. 2008), the 1-km model solution, and the 3-km solution that provided subtidal boundary conditions are compared in Fig. 2. In both models, the geometry of the SST front is approximately correct, particularly the location of the coastal jets separated from the coast near 45° and 42°N in July and August.

To verify the accuracy of the alongshore shelf currents, we utilize acoustic Doppler current profiler (ADCP) velocity data at three midshelf locations on the Oregon shelf [NH10 at 44.66°N, 124.31°W (Kosro 2003); Coos Bay (CB) at 43.16°N, 124.57°W (B. M. Hickey et al. 2009, unpublished manuscript); and Rogue River at 42.44°N, 124.57°W (Ramp and Bahr 2008)]. The depths of these three moorings are 81, 100, and 76 m, respectively, and their locations are shown in Figs. 1 and 2. Time series of depth-averaged, 40-h low-pass-filtered meridional velocities at each location are shown in Figs. 3b–d, including observed velocities (solid black) and model velocities from the smoother (solid half tone) and rougher (dashed half tone) bathymetry solutions. Table 1 shows the mean and standard deviation of each time series as well as model–data root-mean-square difference, complex correlation amplitude CC, and complex phase angle α (Kundu 1976),

$$\mathrm{CC} = \frac{\langle w_1^*(t)w_2(t)\rangle}{\langle w_1^*(t)w_1(t)\rangle^{1/2}\langle w_2^*(t)w_2(t)\rangle^{1/2}}$$
$$= |\mathrm{CC}|e^{i\alpha}.$$

Here, $w_k(t) = u_k(t) + iv_k(t)$; u and v denote zonal and meridional velocity components, respectively; and $\langle \cdot \rangle$ denotes time averaging. To compute correlations, time-averaged values are subtracted. The phase angle is a

TABLE 2. The mean of the major axis amplitude (m s^{-1}) and mean and standard deviation ($\mu \pm \sigma$) of the angle of inclination (relative to due east) of observed and modeled depth-averaged M_2 tidal currents at the NH10, CB, and RR moorings. Standard deviation of the major axis amplitude is small (<0.01 m s^{-1}). For both observed and modeled velocities, the depth average is taken only over the depths at which observations are available. Statistics are computed from harmonic constants from 29 time windows.

	NH10		CB		RR	
	Obs	Model	Obs	Model	Obs	Model
Major axis amplitude (m s^{-1})	0.04	0.04	0.06	0.05	0.05	0.07
Inclination	$73° \pm 3°$	$62° \pm 8°$	$67° \pm 6°$	$67° \pm 6°$	$102° \pm 6°$	$102° \pm 3°$

measure of the average veering between the two vector time series. Based on these comparisons, both models reproduce velocity variability on temporal scales of several days and longer qualitatively correctly at all three locations. One aspect of the observed flow at the Rogue River site, south of Cape Blanco, is large-amplitude variability on time scales of 3–5 days, particularly during the first half of the study period (see Fig. 3d). This is not reproduced in the 1-km model runs, nor is it reproduced in the 3-km model used to provide subtidal boundary conditions. Koch et al. (2010) note that this variability may be due to remote forcing south of the 3-km model domain (40.6°N). Model–data discrepancies over days 210–230 (Coos Bay; Fig. 3c) and 185–210 (Rogue River; Fig. 3d) can be associated with large-scale eddies in the adjacent interior ocean affecting the offshore displacement of the upwelling front.

b. Tidally forced flows

To ensure that the forcing of baroclinic flow is correct, barotropic tides from the three-dimensional 1-km model are compared to the solution from the shallow-water tidal model used to provide boundary conditions. The M_2 sea surface elevation tidal amplitude and phase in both models are consistent over the entire 1-km model domain (Figs. 4a,b). The barotropic M_2 tide propagates from south to north along the coast as a shelf-modified Kelvin wave. It takes approximately 1 h for the barotropic M_2 tide to propagate along the Oregon coast. The sea surface elevation amplitude increases from about 0.6 m in the south to 0.85 m in the north. Figure 4c shows a close-up of the amplitude and phase map over a part of the shelf region and also includes barotropic tidal current ellipses. Here and throughout the entire paper, shaded (clear) ellipses indicate counterclockwise (clockwise) rotation. In the deep water, the tidal current ellipses are strongly polarized and roughly parallel to the coast, with a maximum current velocity of about 0.05 m s^{-1}. Over the slope and shelf (defined here as areas shallower that 200 m; see black contour in the figure), the current ellipses can cross isobaths. In particular, the barotropic current flows over the southern flank of Heceta Bank (43.8°N), suggesting

that this might be an area of intensified internal tide generation.

Next, we verify the accuracy of the modeled baroclinic M_2 internal tide. A point-by-point match between observed and modeled internal tide phase and amplitude can be hard to achieve because of the short horizontal scales associated with internal waves and sensitivity to many model aspects. Here, we are primarily interested in whether modeled internal tide current amplitudes and vertical structures are comparable to the observations on average over the season. For the 2002 study period, 1-h-temporal-resolution velocity profiles, suitable for tidal analysis, are available from the NH10, Coos Bay, and Rogue River moorings. To provide additional evidence about baroclinic tidal variability, we will also use ADCP data from the 2001 Coastal Ocean Advances in Shelf Transport (COAST; Boyd et al. 2002) field program. Data are not available at distances of 10–20 m from the surface and the bottom because of ADCP limitations. For consistency with the observations, model currents are sampled at the same depths and the barotropic velocity is computed as the average over these depths. Tidal harmonic constants are estimated in a series of overlapping 16-day windows offset by 4 days and results are presented as horizontal baroclinic tidal current ellipses (Figs. 5, 7, 9, 11). The upward (rightward) direction in the plots corresponds to the northward (eastward) velocity direction; the line from an ellipse center shows velocity direction at zero phase.

At NH10 (Fig. 5), observed and modeled horizontal baroclinic tidal ellipses are plotted every 4 m in the vertical, at every other observation depth. Barotropic currents are plotted at the top of each panel. They vary in time, but not as much as baroclinic currents. Means and standard deviations of modeled and observed barotropic tidal currents are similar (Table 2). First-mode baroclinic structure is apparent in both the observations (Fig. 5, top) and the model (Fig. 5, bottom), with relatively larger currents and opposite phases near the surface and bottom. The largest observed (modeled) baroclinic current is 0.10 m s^{-1} (0.06 m s^{-1}). Both the modeled and observed series exhibit similar intermittency. There could be several reasons for our model estimates of baroclinic
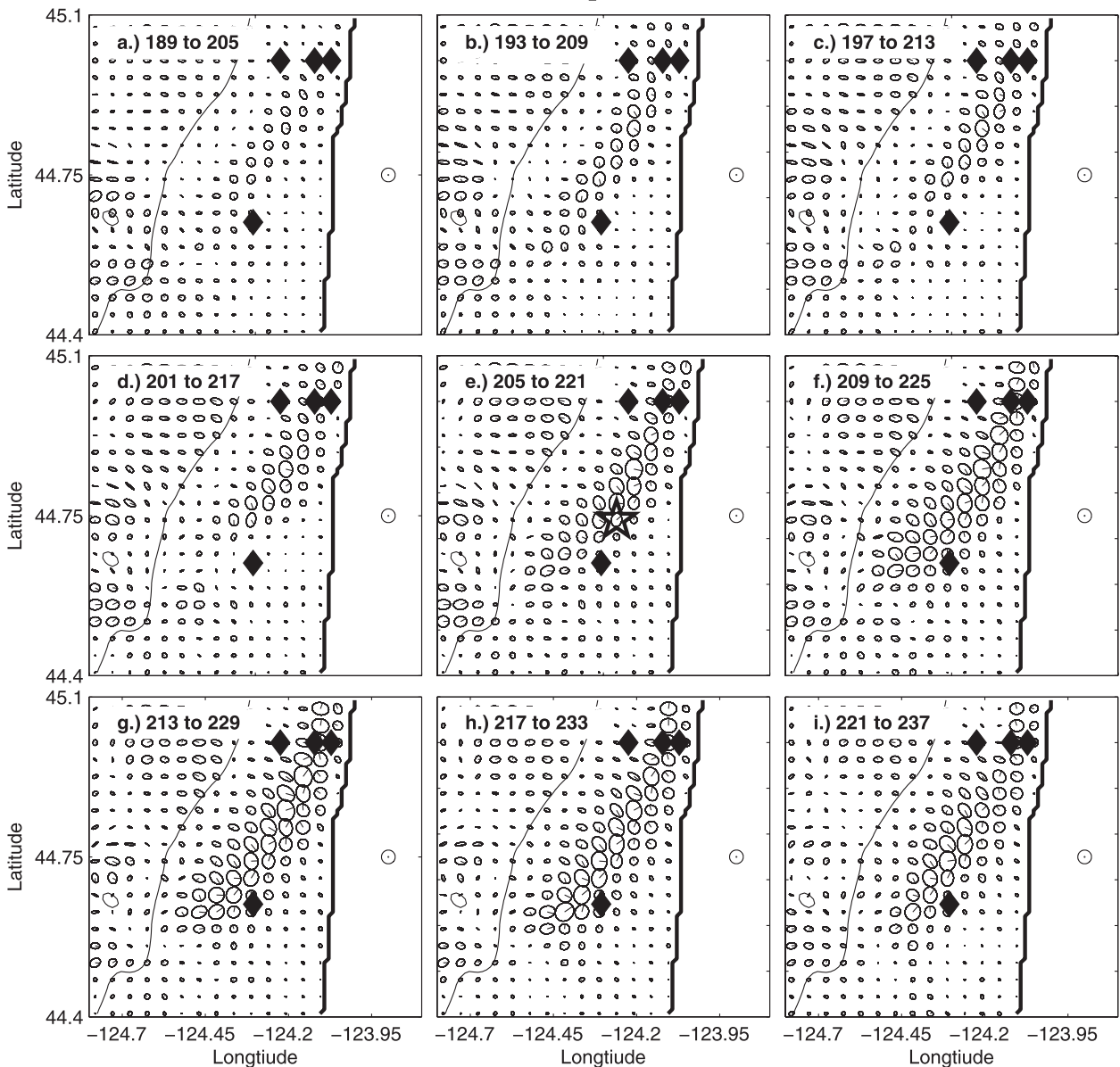
Baroclinic Surface M$_2$ Horizontal Tidal Ellipses

FIG. 6. Modeled surface baroclinic M_2 tidal ellipses near NH10, analyzed in nine consecutive overlapping 16-day windows, yeardays 189–237, a period of observed intensified internal tide near NH10. The scale circle, plotted over land, is 0.1 m s^{-1}. The 200-m isobath is plotted. The black diamonds indicate the location of the NH10 mooring and three moorings from the 2001 COAST experiment. (e) The black star marks the mooring location in Fig. 7. Shaded (unshaded) ellipses indicate counterclockwise (clockwise) rotation. Ellipses are plotted with 4-km horizontal resolution.

tides to be smaller than those observed. For instance, observed current variability in the tidal frequency band may be partially driven by high-frequency atmospheric forcing, which was filtered in the model forcing. Also, the model does not account for the internal tide possibly propagating into our domain.

To further investigate the strength of the baroclinic tide near NH10, a series of surface maps of model baroclinic tidal current ellipses are shown in Fig. 6. For clarity, the ellipses are plotted every 4 km. The black diamond symbol near the center of each panel marks the NH10 mooring. The time period analyzed (days 189–237) corresponds to a period of intensified observed internal tide at NH10 (cf. Fig. 5). During this time period, a region of intensified baroclinic surface tide (with surface current amplitudes > 0.10 m s^{-1}) is found in the
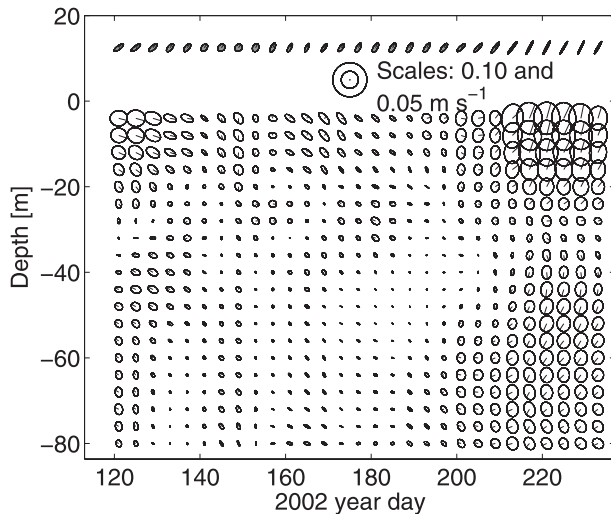
FIG. 7. Model solution baroclinic tidal ellipses at (44.74°N, 124.26°W), approximately 10 km north of the NH10 mooring. Depth is 83 m. Details as in Fig. 5.

FIG. 8. (top) Observed and (bottom) modeled solution baroclinic tidal ellipses at the CB mooring ($h = 100$ m). Details as in Fig. 5.

model at distances of only 4–10 km north and west of NH10. It is possible that small changes in bathymetry or other model details could bring the area of the intensified internal tide closer to the NH10 location.

To see if the internal tide in the region of intensification is similar to observations at NH10, baroclinic tidal ellipses from a location 10 km north of NH10 (marked with a star in Fig. 6e) are shown in Fig. 7. The depth of this location (83 m) is close to that of NH10 (81 m). During days 200–240, both modeled and observed baroclinic currents show first-mode structure with tidal velocities of similar magnitude, roughly 0.10 m s^{-1}. Overall, we conclude that the model solution produces internal tide currents in the NH10 region at magnitudes similar to those observed at the mooring (up to 0.10 m s^{-1}), though not necessarily at the same time.

Analysis of tidal currents at the Coos Bay mooring leads to similar conclusions about the strength of internal tides on the Oregon shelf. In Fig. 8, horizontal tidal ellipses at the Coos Bay mooring are plotted every 6 m in the vertical, one-third the observed resolution. Observed and modeled depth-averaged currents are similar (Table 2). The largest observed (0.12 m s^{-1}) and modeled (0.10 m s^{-1}) internal tide currents are also similar. First-mode baroclinic structure is apparent.

Observed and modeled baroclinic tidal ellipses at the Rogue River mooring location are shown in Fig. 9. Ellipses are plotted every 4 m in the vertical, at the observed resolution. Modeled M_2 internal tide currents (maximum amplitude of 0.06 m s^{-1}) are also generally a bit stronger than observed (maximum amplitude of 0.04 m s^{-1}),
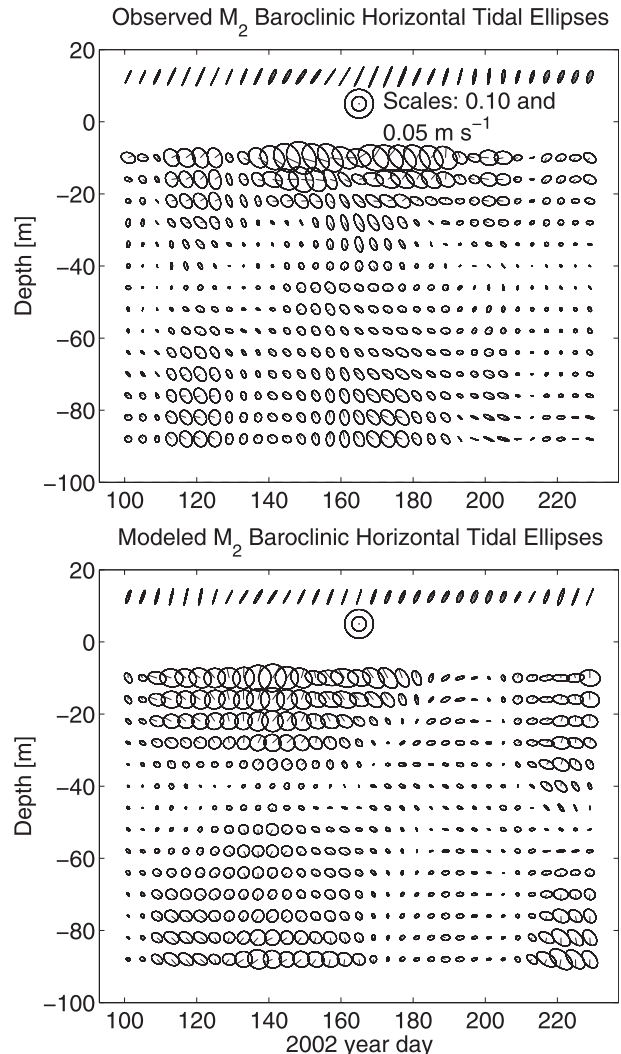
though both are weak compared to barotropic currents (Table 2). Figure 10 shows model baroclinic surface tidal current ellipses in the region around the Rogue River mooring. The mooring location, marked with a black diamond symbol, is in a region of generally weak surface baroclinic M_2 tides, whereas regions of stronger baroclinic tide activity (with currents > 0.10 m s^{-1}) are found to the north and south. Explanations for this pattern are given later, in section 5a.

To develop better understanding of internal tide energetics in the area, we also provide additional analysis of mooring observations from the 2001 COAST experiment (Boyd et al. 2002; Fig. 11). Mooring locations are shown in Fig. 6 as black diamonds along 45°N. At the shallowest and middepth moorings, observed currents

Observed M$_2$ Baroclinic Horizontal Tidal Ellipses

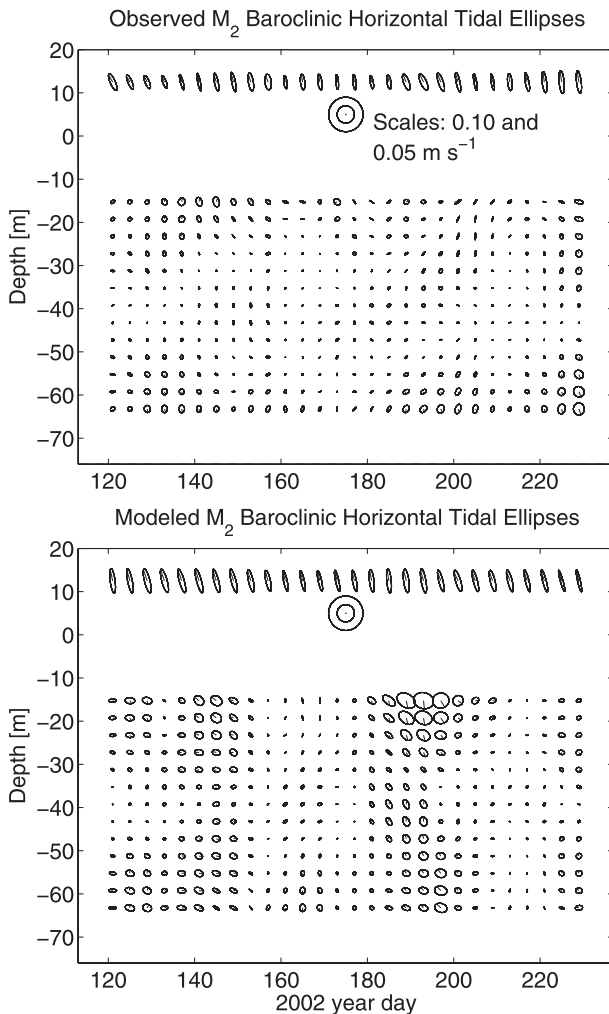Modeled M$_2$ Baroclinic Horizontal Tidal Ellipses

FIG. 9. (top) Observed and (bottom) modeled solution baroclinic tidal ellipses at the RR mooring ($h = 76$ m). Details as in Fig. 5.

are predominately first mode and surface intensified, reaching 0.15 m s^{-1}. At the deepest mooring, first-mode structure is occasionally observed. Measured currents reach 0.10 m s^{-1} at that location. Although background conditions in 2001 and 2002 are likely different, these additional data provide further evidence that M_2 internal tide currents with magnitudes above 0.10 m s^{-1} are not uncommon on the Oregon shelf.

Based on these comparisons, we conclude that the magnitude and variability of the modeled internal tide are qualitatively similar to the observed internal tide. At the same time, the exact timing and location of areas of intensified internal tide are difficult to predict. Further, conclusions about the strength and variability of the M_2 internal tide in a given area based on data from a single mooring may be inaccurate. For a rigorous,

point-by-point analysis of the internal tide, a large number of observations is needed over both the shelf and slope. Analysis of high-frequency radar surface currents (O'Keefe 2005; Kurapov et al. 2003) may provide additional insights and is planned for the future.

4. Baroclinic M_2 tide energetics

a. Stable and intermittent features of M_2 internal tide energetics

In the description below, barotropic (depth averaged) quantities are given subscript 1 and baroclinic quantities are given subscript 2. Based on the linear theory (Kurapov et al. 2003), the depth-integrated, tidally averaged energy balance for the harmonically varying ocean is approximately

$$\text{TEC} \approx \mathbf{V} \cdot \mathbf{EF} + \text{Residual}, \tag{1}$$

where

$$\text{TEC} = \frac{1}{2}\text{Re}\{\tilde{p}_2^*|_{z=-h}\tilde{w}_1\} \quad \text{and} \tag{2}$$

$$= -\frac{1}{2}\text{Re}\{\tilde{p}_2^*|_{z=-h}\tilde{\mathbf{u}}_1\} \cdot \mathbf{V}h \tag{3}$$

is the topographic conversion of barotropic to baroclinic tidal energy and

$$\mathbf{EF} = \frac{1}{2}\int_{-h}^{0} \text{Re}\{\tilde{\mathbf{u}}_2\tilde{p}_2^*\}\, dz \tag{4}$$

is the depth-integrated baroclinic tidal energy flux (**EF**) vector. In (2)–(4), the tilde denotes complex harmonic constants, the asterisk complex conjugates, $w_1 = -\mathbf{u}_1 \cdot \mathbf{V}h$ is the bottom vertical velocity associated with barotropic tidal flow over bathymetry, $\mathbf{u}_1 = (u_1, v_1)$ is the depth-averaged horizontal current vector, $h(x, y)$ is bottom topography, and p_2 is baroclinic tidal pressure, computed as the deviation from the depth-averaged pressure, associated with tidal motions. The residual term accounts for the effects of bottom friction, eddy dissipation throughout the water column, and nonlinear advection effects. In our study, it is not directly computed, but rather estimated as TEC $- \mathbf{V} \cdot \mathbf{EF}$.

Tidal harmonic constant estimates of $\tilde{u}$, $\tilde{v}$, and $\tilde{p}$ are obtained in 16-day time windows offset by 4 days, resulting in 34-point (148 day) time series of **EF** and TEC at each horizontal location. To provide an illustration of M_2 internal tide intermittency, **EF** vectors are shown over a portion of the Oregon shelf from three partially overlapping time windows, yeardays 193–225 (Fig. 12).

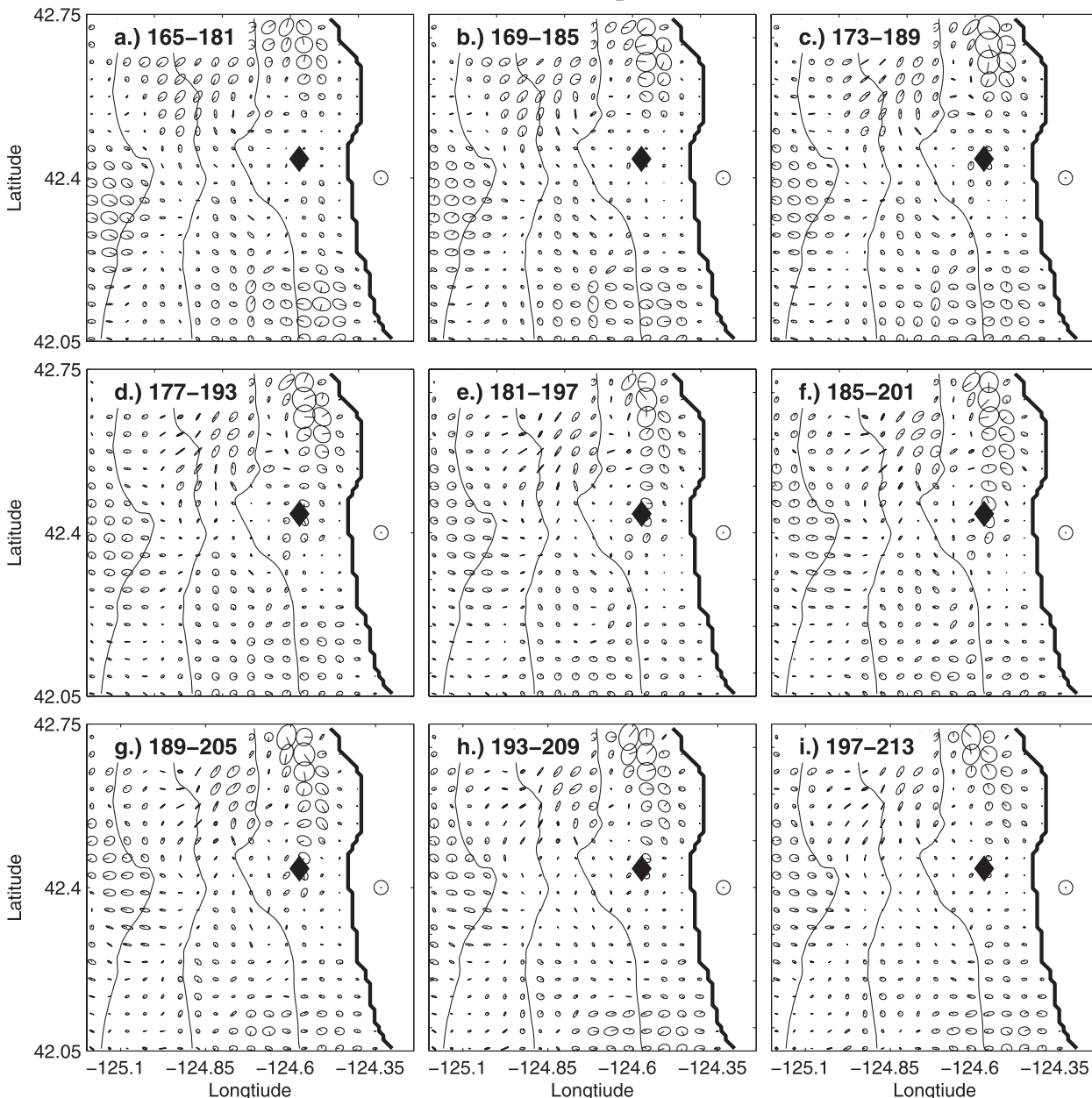Baroclinic Surface M_2 Tidal Ellipses

FIG. 10. Surface baroclinic M_2 tidal ellipses near Rogue River, analyzed in nine overlapping 16-day windows (offset by 4 days), yeardays 165–213. The scale circle, plotted over land, is 0.1 m s^{-1}. Black contours are 200-, 1000-, and 2000-m isobaths. The diamond marker is the location of the RR mooring. Shaded (unshaded) ellipses indicate counterclockwise (clockwise) rotation. Ellipses are plotted with 4-km horizontal resolution.

The onshore flux near 45°N increases over this period. The rectangle shown in each panel of Fig. 12 marks the computational domain in Kurapov et al. (2003). In that study, the M_2 internal tide was modeled using a linear baroclinic model and variational assimilation of high-frequency radar surface currents, with correction of baroclinic tidal fluxes along the open boundary. Both studies find that the M_2 baroclinic tidal energy flux into the smaller domain is from the northwest on average and is $O(10$ W m$^{-1})$. Note that internal tides in the 2003 study were driven by the assimilated data, and the sources of the internal tide propagating into this area were unknown. Here, we can identify the sources within our larger study area.
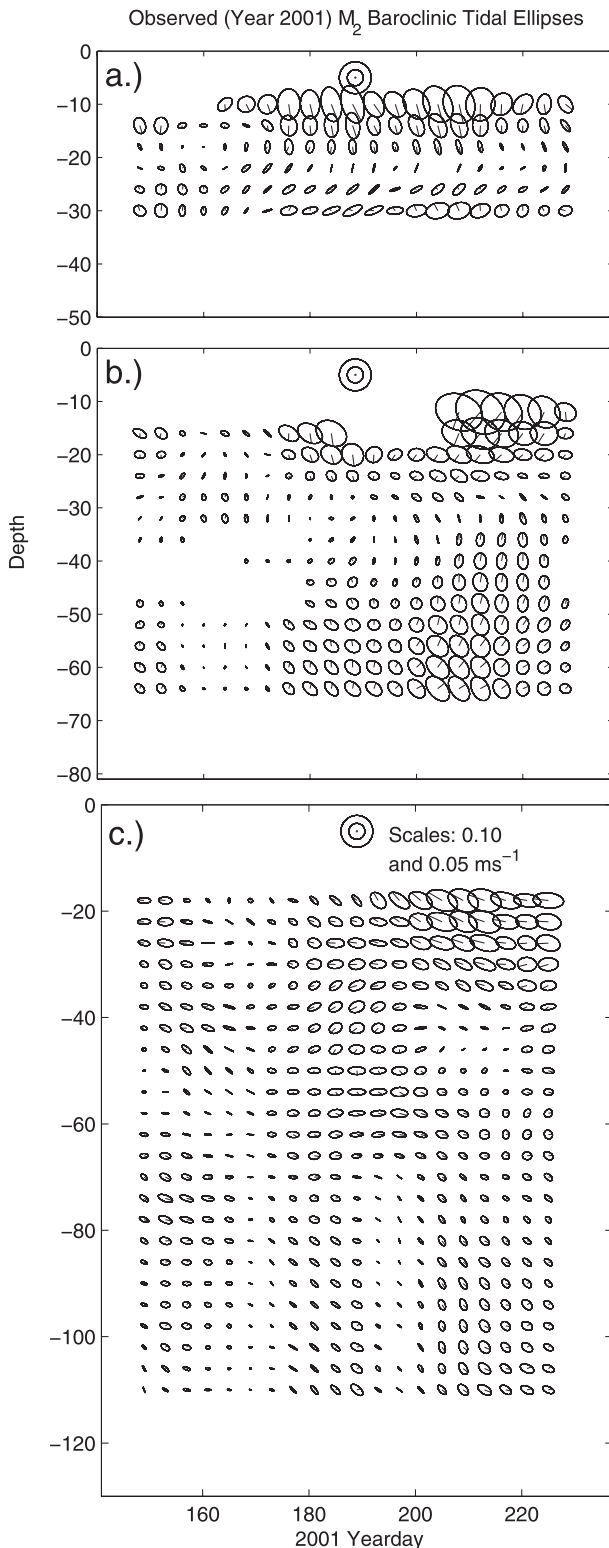
Observed (Year 2001) M$_2$ Baroclinic Tidal Ellipses

FIG. 11. Observed baroclinic tidal ellipses during 2001 at the three COAST moorings along 45°N: depths of (top)–(bottom) 50, 81, and 130 m.

Stable features and intermittency in **EF**, TEC, $\mathbf{V} \cdot \mathbf{EF}$, and the residual are described next using their time-mean and standard deviation maps. Over the slope, the magnitude of the depth-integrated M_2 baroclinic energy flux is $O(100 \text{ W m}^{-1})$ (Fig. 13a; vectors shown every 6 km). Zones of strong **EF** divergence are apparent. At (42.6°N, 124.75°W), in the area near Cape Blanco, the **EF** magnitude approaches 700 W m^{-1}.

To better see smaller **EF** vectors over the shelf ($h < 200$ m), the scale in Fig. 13b is adjusted and vectors are shown every 4 km. At the shelf break ($h = 200$ m), the time-averaged **EF** is directed onshore everywhere, reaching 40–60 W m^{-1} in some places and decreasing toward the coast. Areas of relatively larger onshore **EF** occur near Cape Blanco (42.8°–43°N), along the southern flank of Heceta Bank (43.5°–44°N) and over a wider shelf portion north of 45.2°N. The shelf between 44.2° and 45°N, studied by Kurapov et al. (2003), turns out to be an area of relatively weak onshore **EF**. **EF** standard deviation ellipses over the shelf are shown at 8-km resolution (Fig. 13c). They are polarized, showing maximum variability in the direction of the mean flux. Standard deviation maxima are close to the mean values at the corresponding locations, indicating that the baroclinic tidal flux (mean $\pm$ standard deviation) is mostly onshore. We also find that **EF** over the shelf is weak within about 20 km of the Rogue River mooring (42.44°N) but is much stronger north and south of this shadow zone, similar to the pattern of baroclinic surface tides in Fig. 10.

The map of seasonally averaged TEC (Fig. 14a; color bar limits set at ± 0.04 W m^{-2}) reveals a few hot spots of strong positive TEC. Several small areas of relatively weak negative TEC can also be seen. Formally, this implies that energy is transferred from baroclinic to barotropic tides, although areas of negative TEC may also reflect the difficulty in choosing appropriate definitions of barotropic and baroclinic motions (see Kurapov et al. 2003). Contrary to our expectations, the area south of Heceta Bank (43.8°N), where bathymetry is nearly perpendicular to the general direction of barotropic tide propagation (cf. Fig. 4), is not the largest hot spot of TEC. Comparison of Figs. 14a and 13a suggests that the increased onshore **EF** in that area is partially due to the **EF** propagation from the hot spot at 44.4°N, going around the southern flank of Heceta Bank.

To estimate the contribution of the few TEC hot spots to the total TEC, we compute $P_{\text{TEC}}(v)$, the proportion of the total area-integrated TEC generated by grid points with $0 < \text{TEC} < v$. The total TEC is determined by integration over the area of Fig. 14a, with negative TEC spots excluded. More formally,
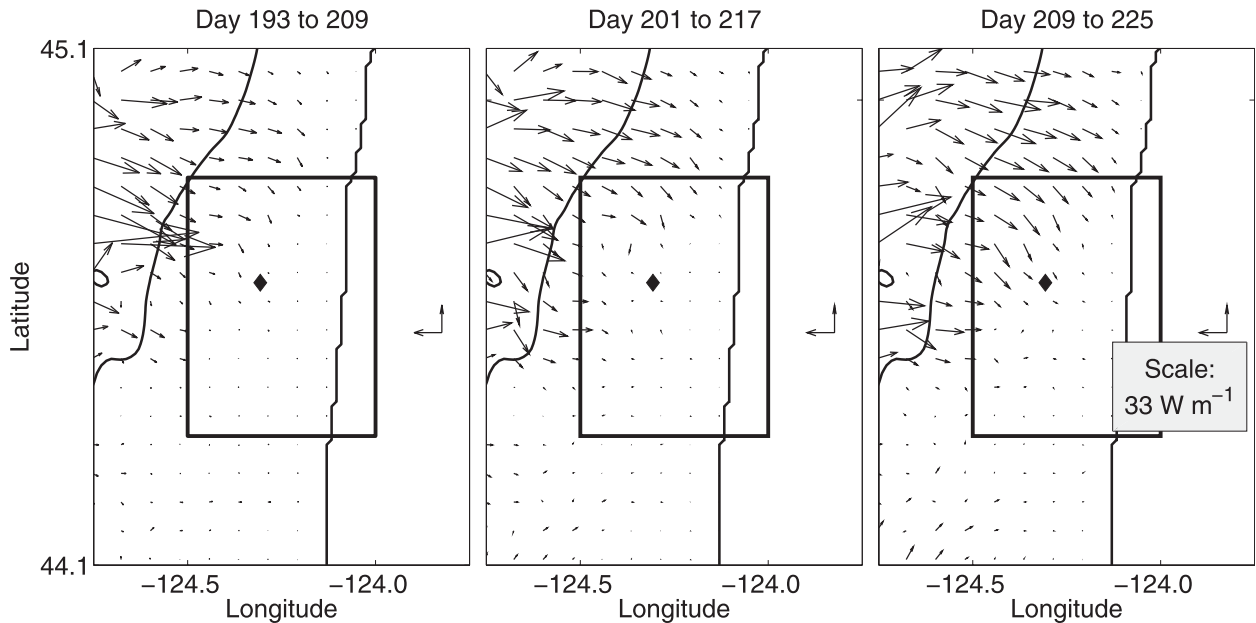
FIG. 12. M_2 baroclinic **EF** vectors analyzed in three partially overlapping 16-day windows over the central Oregon shelf, year-days 193–225. The 200-m isobath contour is shown in black. The rectangle shows the extent of the model domain in Kurapov et al. (2003).

$$\overline{\text{TEC}}(v) = \int_{A(v)} \text{TEC}(\mathbf{x}) \, dA,$$

where $A(v) = \{\mathbf{x} = (x, y) | 0 < \text{TEC}(\mathbf{x}) < v\}$ and

$$P_{\text{TEC}}(v) = \frac{\overline{\text{TEC}}(v)}{\overline{\text{TEC}}(\infty)}. \qquad (5)$$

We find that the hot spots with values greater than 0.04 W m^{-2} contribute approximately 20% of the total TEC (Fig. 15). Interestingly, the combined area of grid cells with TEC ≥ 0.04 W m^{-2} is only 1.2% of the area of the continental slope $(200 < h < 1800$ m). At the same time, about 50% of total TEC is provided by low energy areas with mean values between 0 and 0.015 W m^{-2}. In Fig. 14b, color bar limits are adjusted to ± 0.01 W m^{-2} to emphasize these lower TEC areas. TEC is still patchy and, even at this adjusted scale, is concentrated over selected portions of the slope, with very little baroclinic tidal energy generated over the shelf. TEC standard deviation (Fig. 14c) is also largest over the slope, although its magnitude is generally smaller than the mean. Areas of large TEC standard deviation over the slope are typically associated with large mean values.

To provide further insight about what contributes to spatial variability of TEC, we examine the factors in (2): namely, the time-averaged amplitudes of barotropic

tidal vertical velocity at the bottom $\tilde{w}_1$ (Fig. 16a) and the bottom baroclinic tidal pressure $\tilde{p}_2|_{z=-h}$ (Fig. 16b). Both factors are elevated at TEC hot spots (contoured in gray at 0.02 W m^{-2}). The bottom vertical velocity is affected by finescale bathymetric variations and exhibits spatial variability on smaller scales than the bottom baroclinic pressure. The latter can be associated not only with generation but also with propagation of the internal waves. The horizontal wave lengths on the slope are generally larger than the scales of bathymetric variations resolved by the 1-km model, yielding a smoother baroclinic pressure amplitude field. In particular, the amplitude of $\tilde{p}_2|_{z=-h}$ is elevated in the area west and south of Heceta Bank (43.6°–44.5°N), consistent with the average path of the internal wave energy propagation (see Fig. 13a).

Maps of M_2 baroclinic energy flux divergence ($\mathbf{\nabla} \cdot \mathbf{EF}$; Fig. 17) are analyzed in similar ways. Time-averaged $\mathbf{\nabla} \cdot \mathbf{EF}$ has a few hot spots over the slope (Fig. 17a), typically collocated with the TEC hot spots. At the adjusted scale (Fig. 17b), areas of large divergence on the slope coincide with areas of large TEC (Fig. 14b). The adjusted scale also reveals areas of energy flux convergence (negative divergence), found both over the slope and shelf, which can be associated with internal tide dissipation.

The residual TEC $-\mathbf{\nabla} \cdot \mathbf{EF}$, which we would like to interpret as dissipation, is predominately positive. Maps
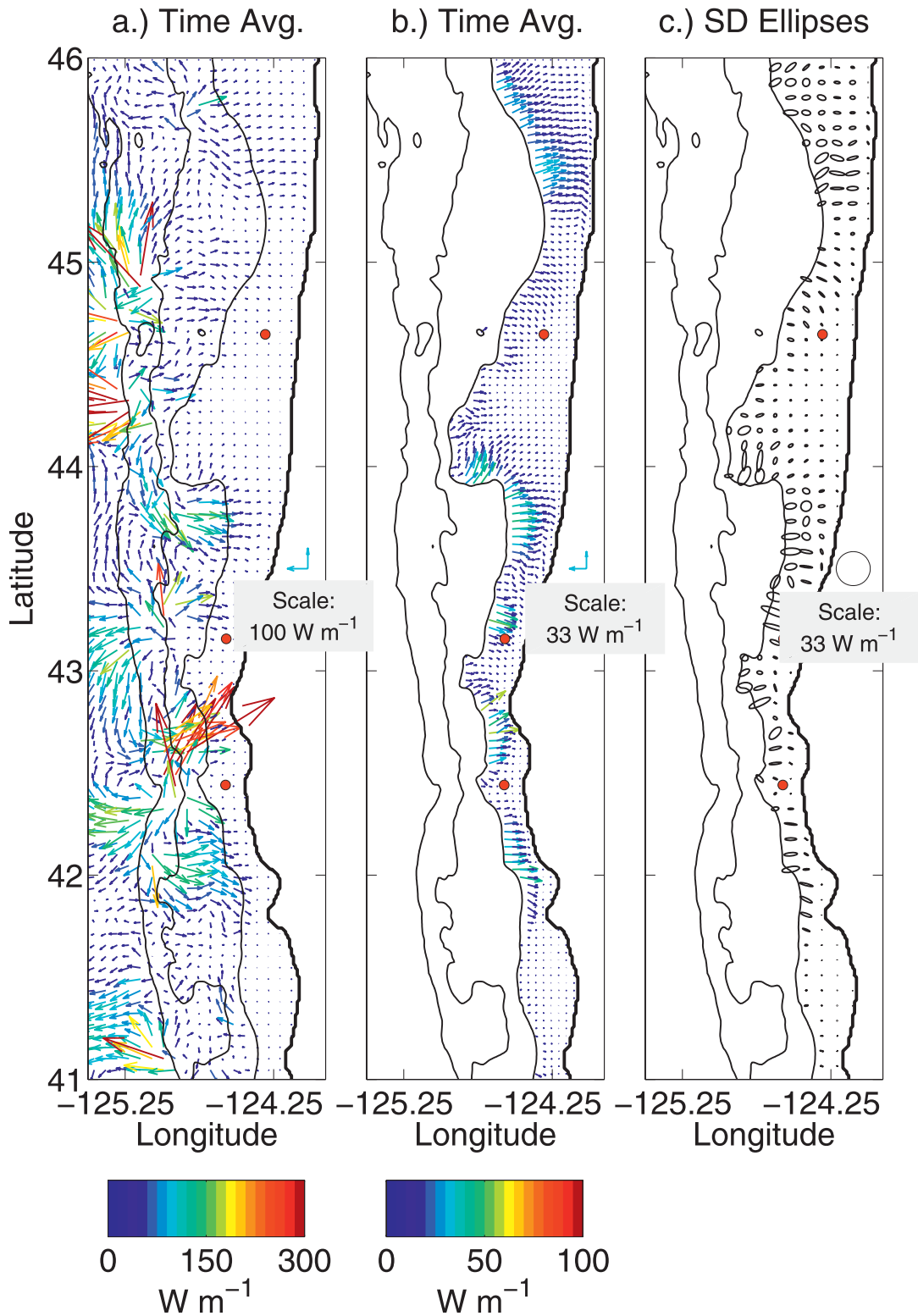
FIG. 13. Time-average and standard deviation ellipses of the M_2 baroclinic **EF**, where color shows **EF** magnitude: (a) **EF** shown every 6 km, with the vector scale and color range (0–300 W m^{-1}) chosen to emphasize **EF** on the slope; (b) **EF** on the shelf shown using a different vector and color scales (0–100 W m^{-1}), for every 4 km; and (c) standard deviation ellipses on the shelf, for every 8 km. Black contours are the 200-, 1000-, and 2000-m isobaths.
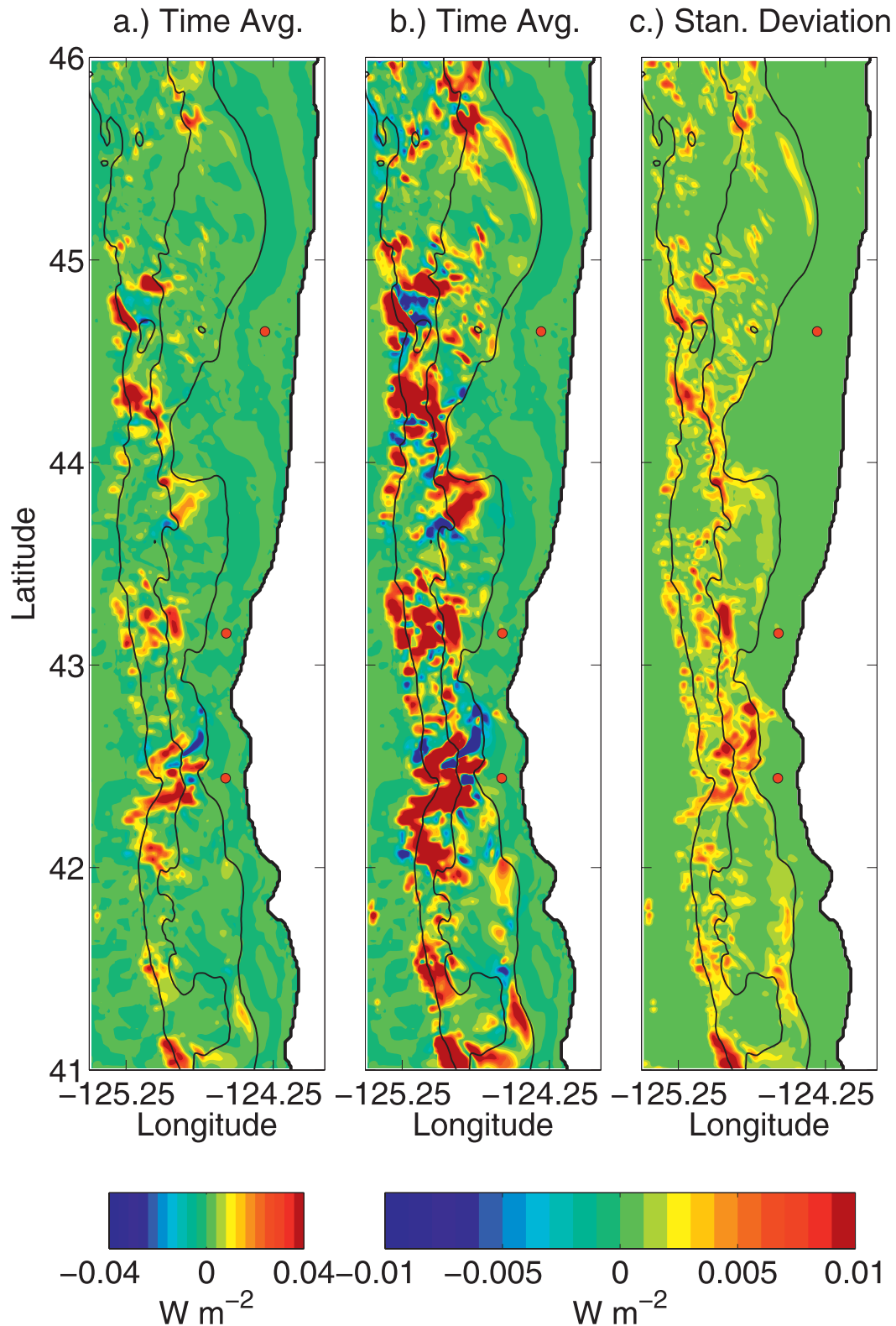
a.) Time Avg.　　　b.) Time Avg.　　　c.) Stan. Deviation

FIG. 14. Time average and standard deviation of TEC: (a) time average, where the color range (± 0.04 W m^{-2}) is chosen to emphasize hot spots; (b) time average at the finer range (± 0.01 W m^{-2}); and (c) standard deviation. Black contours indicate the 200-, 1000-, and 2000-m isobaths.
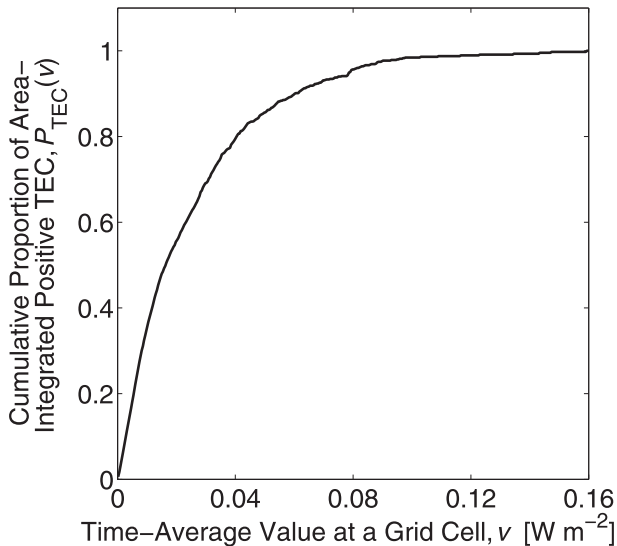
FIG. 15. Proportion of area-integrated positive TEC $P_{TEC}(v)$ [Eq. (5)] below a threshold value v.

of the season-averaged residual (Fig. 18a) reveal that the TEC hot spots (with their edges shown as white contours at the 0.02 W m^{-2} level) are well balanced by $\nabla \cdot \mathbf{EF}$. The map at the adjusted color scale (Fig. 18b) shows vast areas of increased residual over the slope and some over the shelf.

b. Reasons for internal tide intermittency

Internal tide intermittency can result from a number of local and remote factors, including focusing of internal tide rays in a nonuniform medium (Chavanne et al. 2010), variability in TEC associated with changes in stratification around the hot spots (Kurapov et al. 2010) and constructive/destructive interference of remotely generated internal waves (Kelly and Nash 2010). Chavanne et al. (2010) used a ray tracing technique to consider internal wave energy propagation from an underwater ridge in the Hawaiian archipelago and found that a mesoscale eddy can create zones of ray focusing, resulting in areas of larger internal tide signal near the surface. Without a doubt, variability in background conditions affects internal wave propagation in our study area. However, in our case, not only internal tide propagation but also generation varies with time. Because along the Oregon coast major TEC hot spots are located in close proximity, it is hard to interpret whether changes in TEC over a given spot are due to local changes in stratification or remote influence of nearby spots. This remote influence (constructive interference mentioned above; see Kelly and Nash 2010) can be explained using (2). Although w_1 is determined by the local topography

and barotropic tide and is relatively steady, near-bottom p_2 can be influenced by both local generation processes and the baroclinic waves propagating into the area (e.g., from neighboring hot spots). The incoming wave can modify the phase and amplitude of p_2 such that the product $\tilde{w}_1^* \tilde{p}_2$ becomes smaller or larger.

Additional analysis in smaller areas shows that the range of change of TEC can be comparable to the change in the onshore $\mathbf{EF}$ in the vicinity. However, it would not be the only factor determining the amount of onshore $\mathbf{EF}$. For illustration, Figs. 19a,b show maps of $\mathbf{EF}$ and the near-bottom p_2 amplitude in the area south of Heceta Bank in two windows, centered on days 193 and 229. Figure 20 shows the time series of TEC and residual integrated over the slope area (bounded by the edges of the map in Fig. 19 and the 200-m isobath), as well as the integrated $\mathbf{EF}$ across the 200-m isobath and the net $\mathbf{EF}$ through the southern, western, and northern boundaries of this small area. Values corresponding to the selected time windows are marked with circles. The first (second) time window selected in Fig. 19 corresponds to a relatively smaller (larger) onshore $\mathbf{EF}$. The onshore $\mathbf{EF}$ is increased by 2.5 MW between days 193 and 229. This increase is comparable to that in TEC over the same period. A change in the strength of the internal tide is also clearly seen in surface horizontal baroclinic tidal ellipses (Figs. 19c,d). Figures 19a,b suggest that the influence of the hot spot at 44.3°N on p_2 south of Heceta Bank (43.7°N) is smaller in the first time window, days 185–201, than the second window, days 221–237. Remarkably, the residual (dissipation) in the pictured area increases sharply after day 200 (by more than 5 MW), whereas the net outward $\mathbf{EF}$ through the outer boundaries is reduced during the same period. So, despite TEC and onshore $\mathbf{EF}$ changing by similar amounts over days 193–230, we cannot claim that local increases in internal tide generation are solely responsible for the increase in the onshore $\mathbf{EF}$. Influences of remotely generated internal tide complicate analysis of tidal intermittency, making it difficult to establish a definitive relationship with wind-driven conditions.

5. Bathymetric effects on M_2 internal tide energy fluxes

a. Bathymetry criticality

Internal wave energy propagates along wave characteristics (Wunsch 1975; Baines 1982). The angle ϕ that a characteristic makes with the horizontal is determined by

$$\tan\phi = (\omega^2 - f^2)^{1/2}(N^2 - \omega^2)^{-1/2},$$
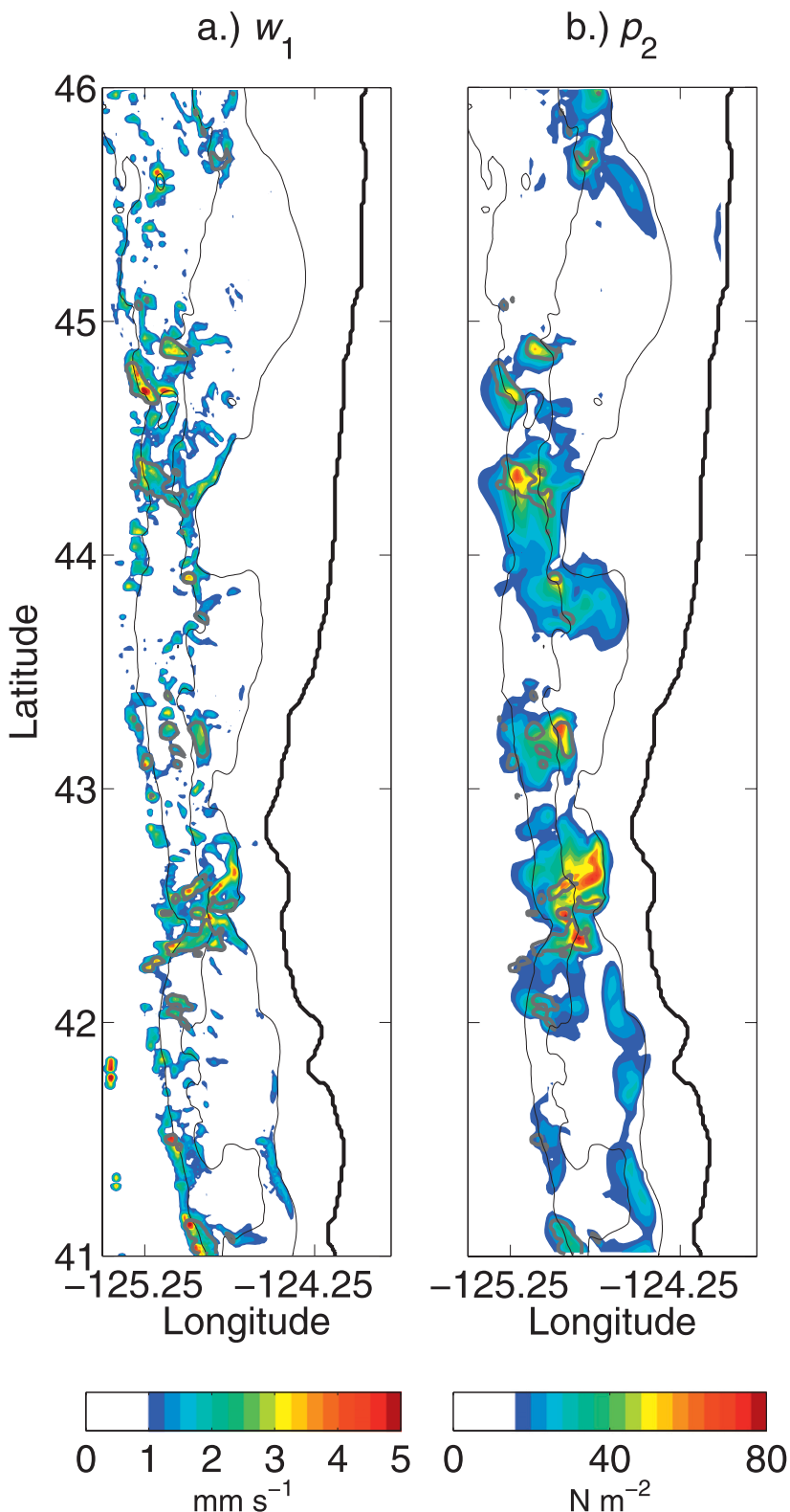
a.) w_1 b.) p_2

FIG. 16. Time-averaged amplitudes of harmonic constants determining TEC [Eq. (2)]: (a) vertical barotropic velocity at the bottom and (b) tidal baroclinic pressure at the bottom. Black contours mark the 200-, 1000-, and 2000-m isobaths. Half-tone contours mark TEC = 0.02 W m^{-2}.
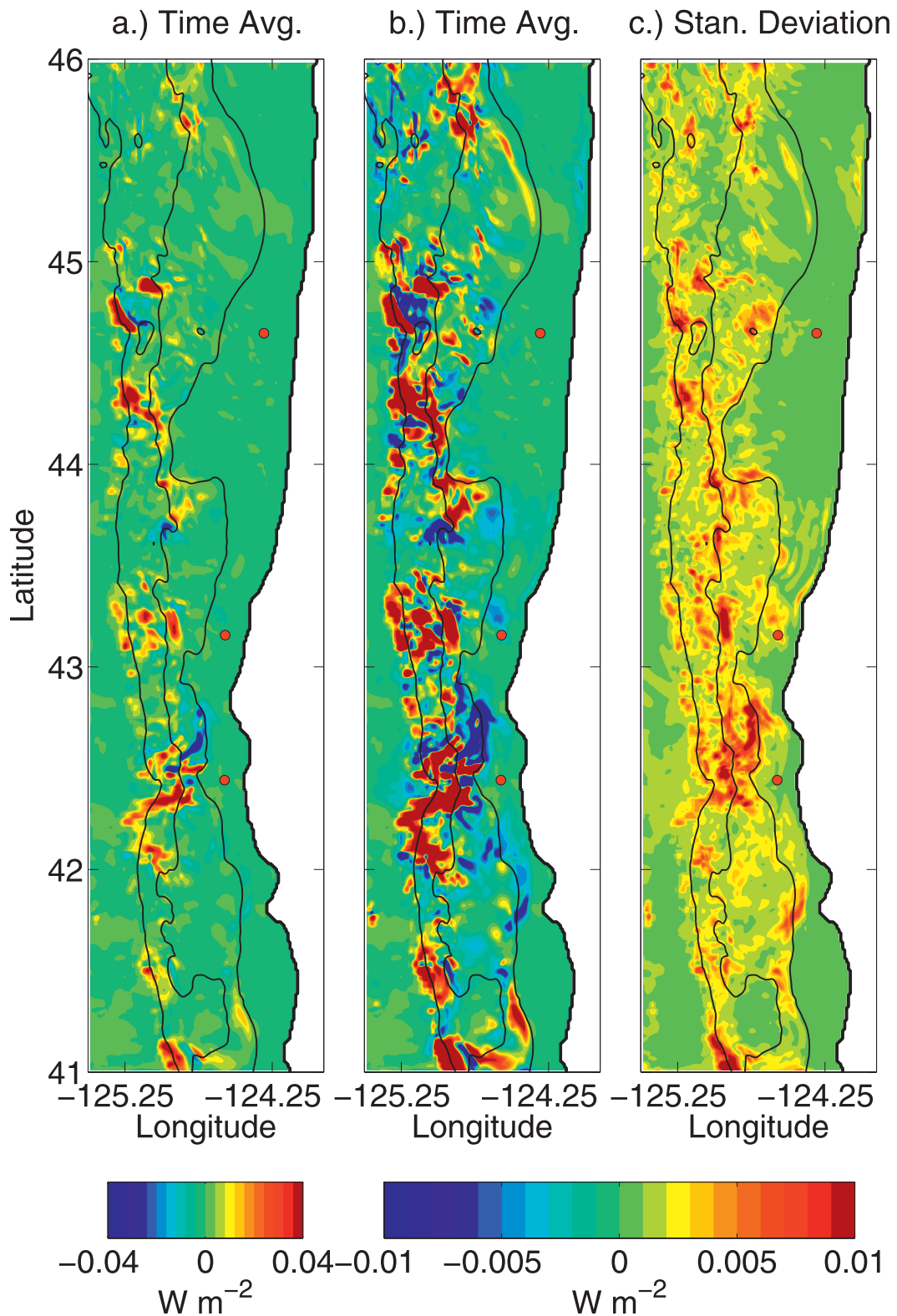
FIG. 17. Time average and standard deviation of the M_2 baroclinic **EF** divergence: (a) time average, where the color range (± 0.04 W m^{-2}) is chosen to emphasize hot spots; (b) time average at the finer range (± 0.01 W m^{-2}); and (c) standard deviation. Black contours are the 200-, 1000-, and 2000-m isobaths.
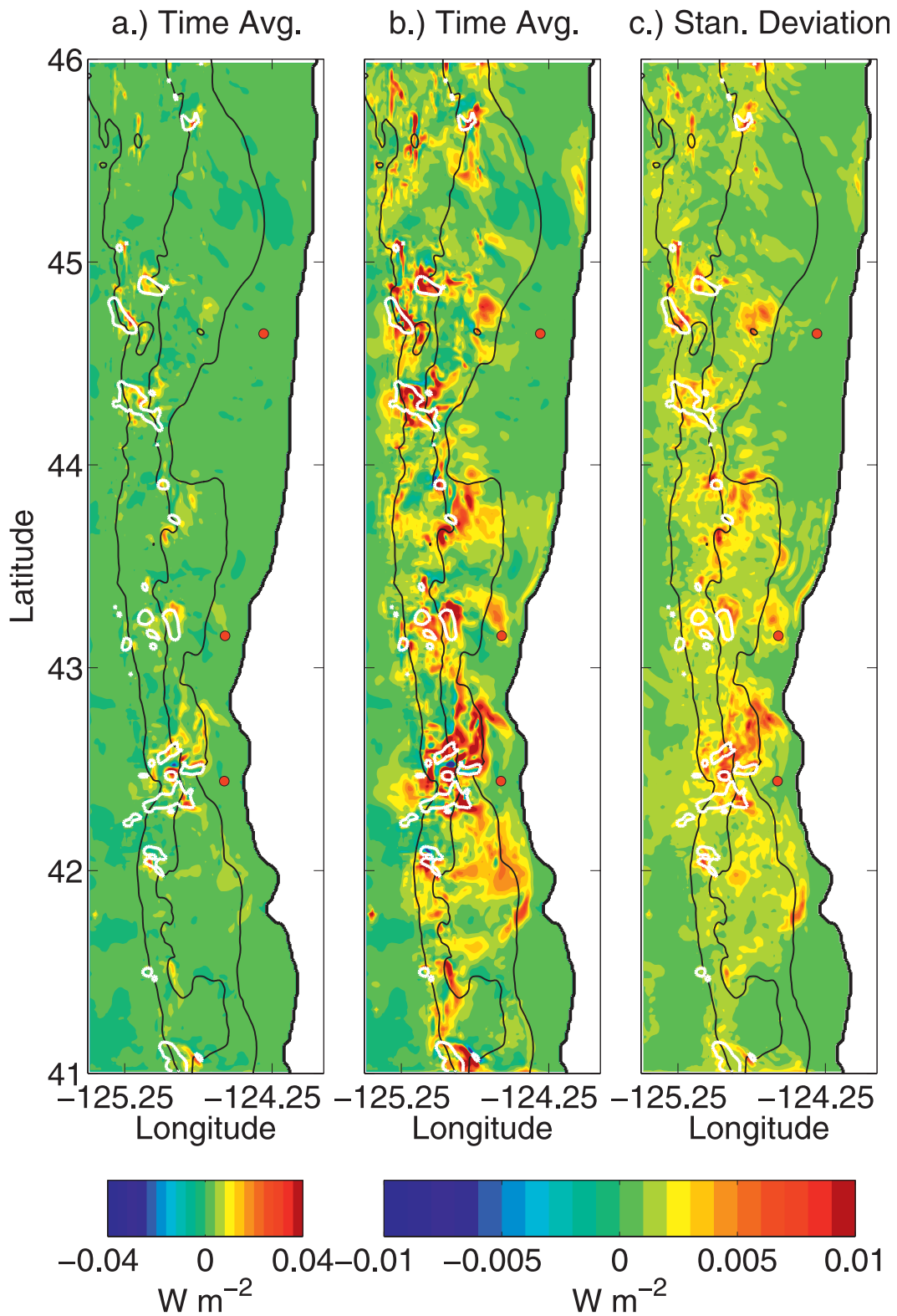
FIG. 18. Time average and standard deviation of the residual in (1): (a) time average, with the color range ± 0.04 W m^{-2}; (b) time average at the finer range (± 0.01 W m^{-2}); and (c) standard deviation. Black contours are the 200-, 1000-, and 2000-m isobaths.
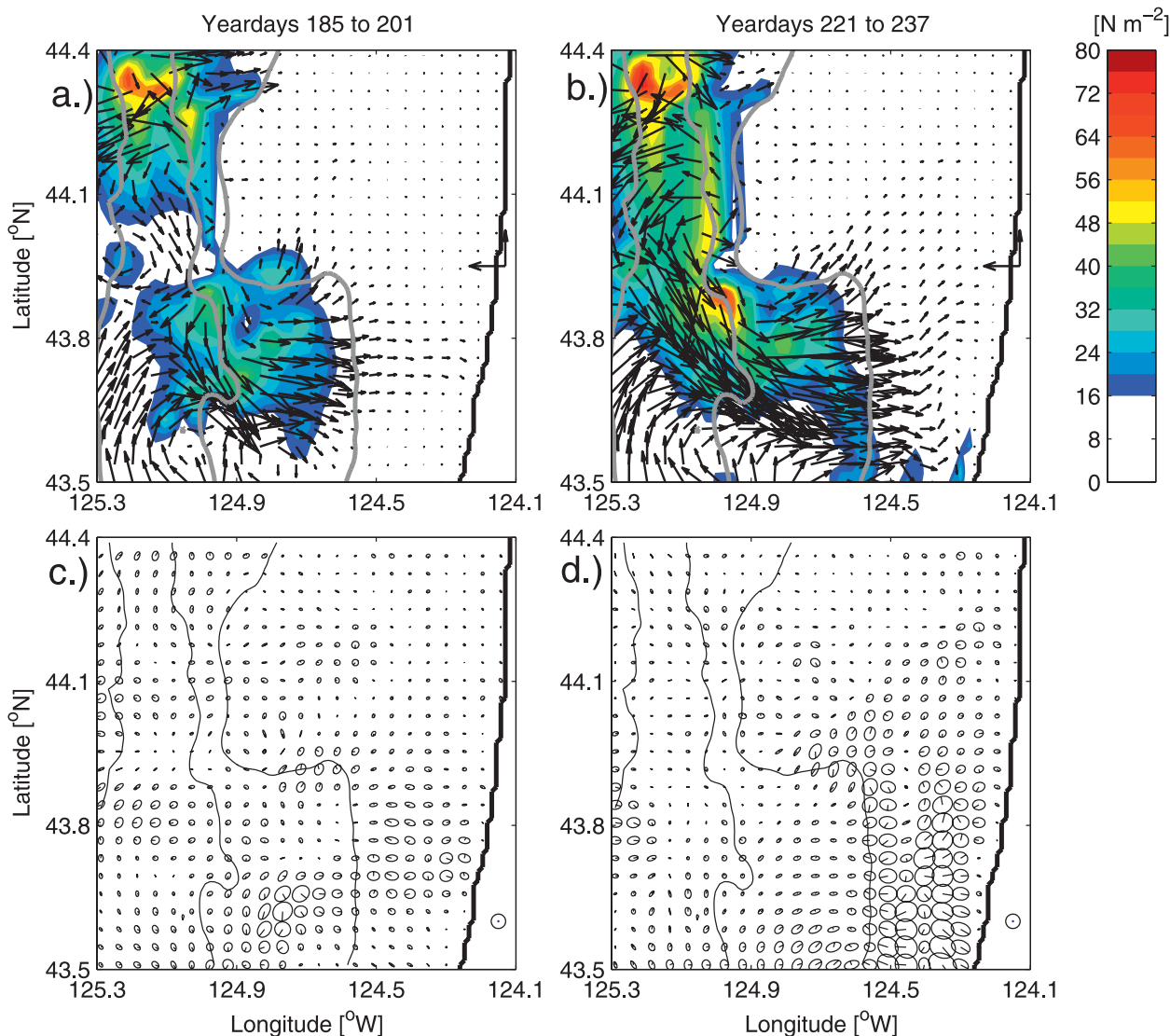
FIG. 19. (top) Depth-integrated, tidally averaged M_2 baroclinic **EF** vectors and bottom baroclinic pressure during yeardays (a) 185–201 and (b) 221–237. The 200-, 1000-, and 2000-m isobaths are contoured in gray. Scale vectors (right of each panel) are 100 W m^{-1}. (bottom) Surface baroclinic tidal ellipses for the corresponding time periods. Scale circle at lower right is 0.10 m s^{-1}. Isobaths are contoured at the same intervals.

where ω is the tidal frequency, f is the inertial frequency, and N is the buoyancy frequency. Internal wave beams incident on a supercritical slope (where the bottom slope $\nabla h = \tan\theta$ is steeper than the characteristic slope $\tan\phi$) reflect toward deeper water, whereas those incident on subcritical bathymetry ($\tan\theta < \tan\phi$) will propagate into shallower water.

To calculate ϕ, the buoyancy frequency is estimated 20 m above the ocean floor using density profiles computed from temperature and salinity averaged over the entire model run. Figure 21 shows a map of the angle difference $\theta - \phi$. On the offshore side of the 200-m isobath, bathymetry varies from subcritical ($\theta - \phi < 0$; blue) to near critical ($\theta - \phi \approx 0$; green) and supercritical ($\theta - \phi > 0$; red). Seasonally averaged **EF** vectors across the 200-m isobath are also plotted in Fig. 21, repeated from Fig. 13. Sections with relatively larger onshore baroclinic tidal **EF** are generally found near areas where bathymetry is subcritical or near critical on the offshore side of the 200-m isobath, such as in the ranges 41.7°–42.2°N and 43.5°–43.9°N. Sections with low onshore energy flux in places where bathymetry is supercritical at the shelf break are also easily identified: for example, in the
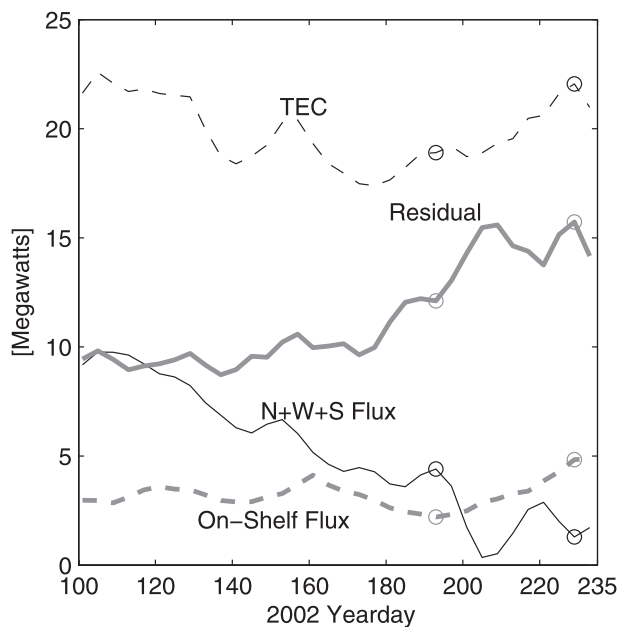
FIG. 20. Time series of energy balance terms for the slope region in Fig. 19 [(125.3°W, 200-m isobath) × (43.5°N, 44.4°N)]. For the flux terms, positive values correspond to energy radiating out of the region. Circles on each line mark yeardays 193 and 229, the midpoints of the windows in Fig. 19.

areas of 41.0°–41.7°N, 42.3°–42.5°N, 42.9°–43.1°N, and 43.9°–44.5°N.

To provide a more quantitative assessment, we consider the correlation between the magnitude of the onshore **EF** across $h = 200$ m and bathymetric criticality in the 10-km band offshore of this isobath. This relationship is complicated by nonuniformity of internal tide energy generation along the slope. For instance, between 44.5° and 45°N, bathymetry is mostly subcritical just offshore of the 200-m isobath, but **EF** here is relatively low, because little baroclinic energy is generated offshore near this area (see Fig. 14b). In contrast, at 42.7°N, where bathymetry is supercritical just offshore of the 200-m isobath, the onshore **EF** is larger than anywhere else along the 200-m isobath, because there is an extremely powerful source nearby, in the deep water at 42.3°N. To account for alongshore variation in generation, the **EF** magnitude at each point on the 200-m isobath is compared to the value at a point 10 km offshore, in the direction normal to the 200-m isobath. Dividing the two values, we obtain the percent ratio of propagated **EF**, which is then compared to the mean of $\theta - \phi$ over the 10-km distance between the two points. Results (Fig. 22, where $\theta - \phi > 0°$ corresponds to supercritical bathymetry) suggest that, in general, relatively less energy propagates onshore through areas of stronger supercritical bathymetry along the shelfbreak rim. Two
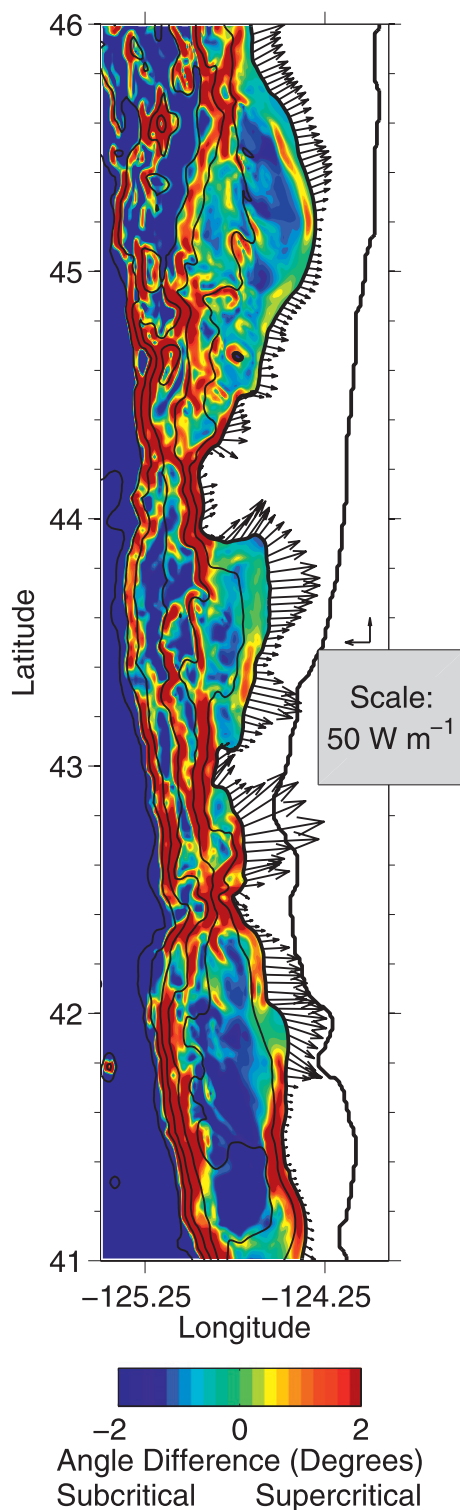

FIG. 21. Bathymetric criticality (bathymetric slope angle minus wave characteristic slope angle), shown over the continental slope (color; shelf omitted), and **EF** across the 200-m isobath (vectors). Positive bathymetric criticality (warm colors) corresponds to the steep, supercritical slope. Thick black contours are the coast and 200-m isobaths. Thin black contours are every 500 m.
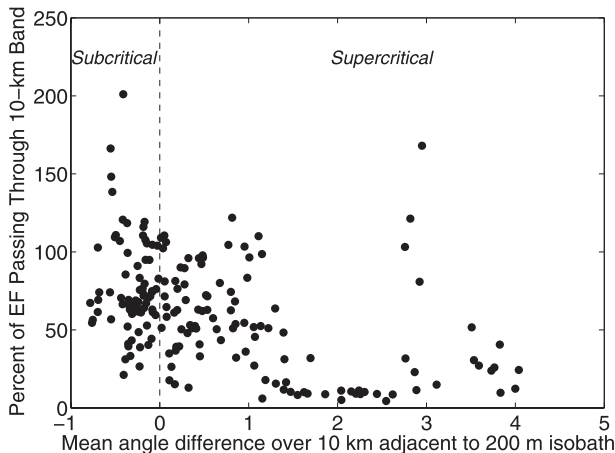
FIG. 22. Scatterplot of the percent ratio of **EF** passing through the 10-km strip offshore of the 200-m isobath vs the mean angle difference (bathymetric slope minus wave characteristic slope). Averaging is in the direction perpendicular to the 200-m isobath. Positive angle difference corresponds to supercritical bathymetry, and negative difference to subcritical bathymetry.

aspects of the plot necessitate further explanation. First, percentages exceed 100% at several locations where substantial internal tide energy is generated in the 10-km band. Second, strips of the supercritical bathymetry do not reflect all the internal tide energy into the deeper water. It is possible that some internal tide energy can propagate over narrow regions of supercritical bathymetry along characteristics that do not touch the slope (e.g., along characteristics that reflect off the surface in those areas).

An example of how bathymetric criticality affects the onshore **EF** and resulting tidal currents is seen in the region surrounding the Rogue River mooring. Between 42° and 43°N, the mean onshore **EF** (Fig. 21) and M_2 tidal currents (Fig. 10) are relatively large, except around 42.4°N. Bathymetry offshore of the 200-m isobath at 42.4°N is supercritical in a 35-km-wide region next to the 200-m isobath. While this region of steep bathymetry is generating a large amount of baroclinic tidal energy (Fig. 14a), the energy is either reflected offshore or propagated to the north and the south of 42.4°N (Fig. 13a), creating a ''shadow'' zone (Fig. 13b) surrounding the Rogue River mooring.

It also appears that regions of relatively large TEC are frequently associated with supercritical bathymetry. A total of 99.75% of TEC hot spot (>0.04 W m^{-2}) area is over supercritical bathymetry, and 87.67% of the area with TEC greater than 0.015 W m^{-2} (the threshold separating the upper 50% of area-integrated positive

TEC activity from the bottom 50%; see Fig. 15) is also found over supercritical bathymetry.

b. Bathymetry roughness and area-integrated energy balance

Figure 23 shows time-averaged, depth-integrated baroclinic **EF** vectors and standard deviation ellipses over the slope and shelf for the smoother bathymetry case. **EF** in the smoother bathymetry case is somewhat weaker, although the spatial distribution of **EF** over the 200-m isobath is similar to that in the rougher bathymetry case (cf. Figs. 13b, 23b). These results are consistent with those of Jachec et al. (2007), who studied tidal circulation in Monterey Bay, California, using models of different resolution.

Another perspective on the energy balance, as well as its sensitivity to bathymetric resolution, is provided by area integration of the terms in (1) over the slope (200 m $< h <$ 1800 m) and shelf ($h <$ 200 m) regions. The time series of these terms are shown for the rougher bathymetry case in Fig. 24. Integration of $\mathbf{V} \cdot \mathbf{EF}$ over the shelf yields the total energy radiating onto the shelf across the 200-m isobath (fluxes across the southern and northern boundaries are neglected). This value does not vary much with time, despite the substantial temporal and spatial variability in the M_2 internal tide over the shelf. There is very little TEC over the shelf, which is consistent with Figs. 14b,c.

Time averages of the area-integrated terms are summarized in Fig. 25, for both the rougher (Fig. 25a) and smoother (Fig. 25b) bathymetry cases. In the rougher bathymetry case (Fig. 25a), the integrated TEC over the slope has a mean value of about 81 MW. About 68% of this, approximately 55 MW, is dissipated over the slope. Integrating $\mathbf{V} \cdot \mathbf{EF}$ over the slope yields the energy radiated out of the area, approximately 26 MW, which is nearly the sum of fluxes into the ocean interior (across the 1800-m isobath) and onto the shelf. About 14 MW is radiated from slope to shelf and about 12 MW is radiated to the interior ocean.

In the smoother bathymetry case (Fig. 25b), baroclinic energy production over the slope is reduced by 34% to 54 MW. Dissipation is reduced by 38% to 34 MW. Thus, the ratio of dissipated to generated internal tide energy remains about the same over rougher and smoother bathymetry, with about 65% of baroclinic energy generated over the slope also dissipated there. In the case of smoother bathymetry, the integrated divergence of **EF** from the slope to the shelf is also reduced (to a total of 11 MW), but only by 18%. It appears that bathymetric resolution affects the levels of internal tide generation and dissipation more than the integrated value of onshore propagating **EF**.
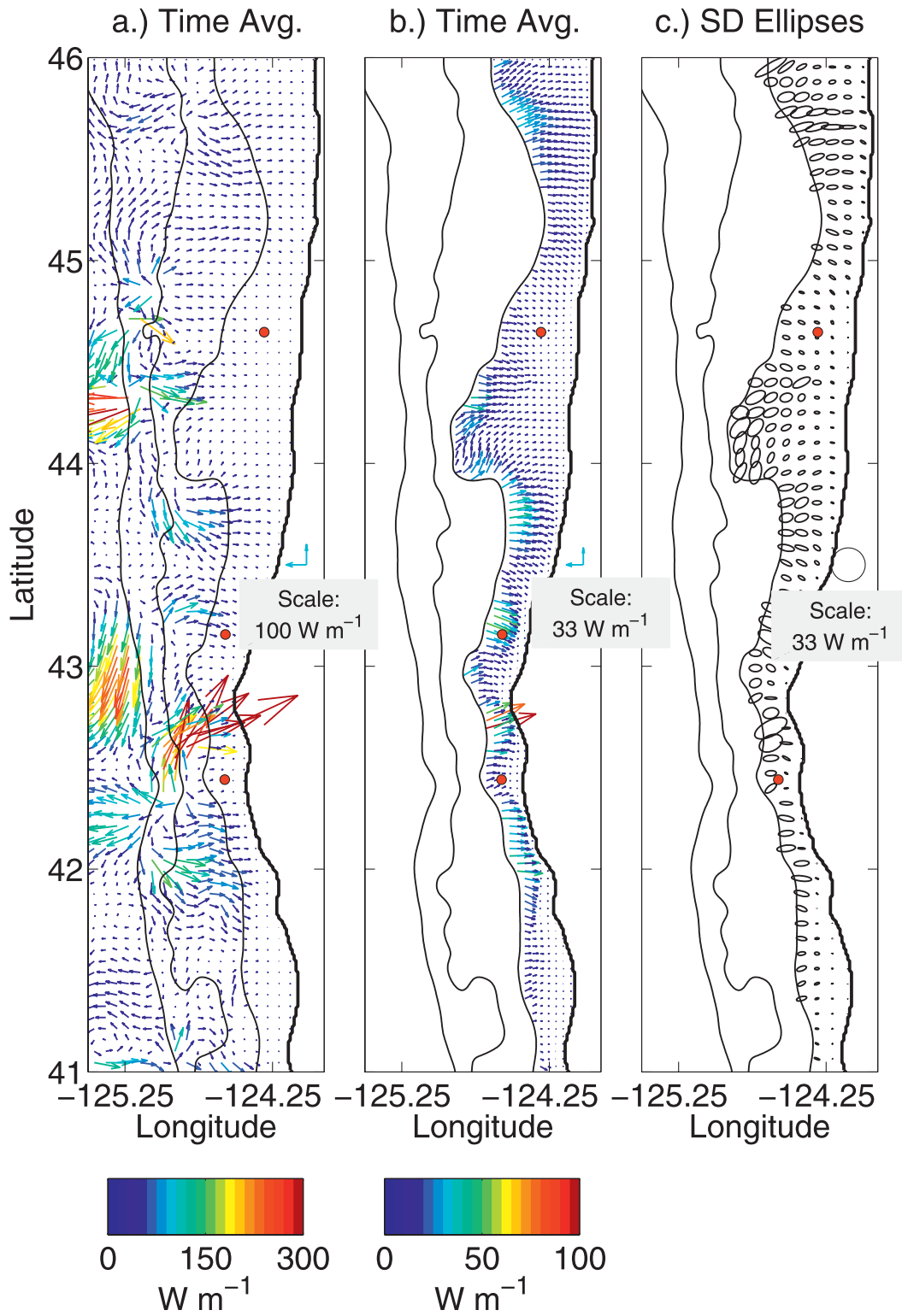
FIG. 23. Time-averaged M_2 baroclinic **EF** vectors and standard deviation ellipses from the smoother bathymetry case. Details as in Fig. 13.
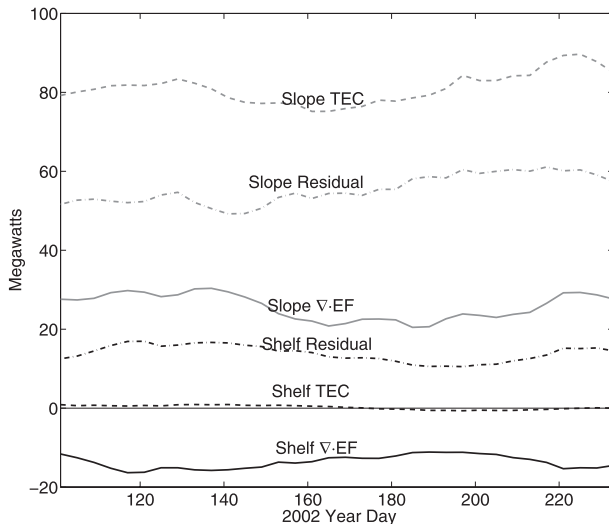
FIG. 24. Time series of the area-integrated TEC, $\nabla \cdot \mathbf{EF}$, and the residual. Half-tone lines are for the area between the 1800- and 200-m isobaths (the slope), and black lines are for the area between the 200-m isobath and the coast (the shelf).

6. Summary

The nested 1-km-resolution model presented here describes coastal ocean circulation off Oregon in both the subinertial (wind driven) and superinertial (semi-diurnal) frequency bands quantitatively correctly. Our study has focused on generation (TEC) and propagation of the superinertial M_2 internal tide in this area. We find that most baroclinic tidal energy is generated over the slope with a few hot spots (occupying 1.2% of the area of the continental slope) contributing 20% of the total TEC.

Variability in both space and time is a prominent feature of the internal tide on the Oregon shelf, reflecting variation in background currents and hydrographic conditions. Although the model describes intermittency in the internal tide qualitatively correctly, the exact locations and times of intensified M_2 internal tide are still difficult to predict. Furthermore, although it is clear that internal tide intermittency is associated with variability in wind-driven circulation, no simple relationship has been found between the intensity of the internal tide and characteristics of upwelling/downwelling, despite our attempts to find such a relationship.

Some aspects of baroclinic M_2 energetics are quite stable. For instance, the locations of TEC hot spots are defined primarily by bathymetric details and are relatively weakly affected by background conditions. Despite day-to-day variability in the onshore baroclinic $\mathbf{EF}$, the net flux onto the shelf, integrated along the 200-m isobath, remains rather steady during the summer season. About 65% of the internal tide energy converted from the barotropic tide over the slope is dissipated on the slope. The remaining energy is propagated both into the interior ocean and onto the shelf, in roughly equal proportions. Spatial variability in the onshore energy flux is controlled to a great extent by bathymetric criticality offshore of the 200-m isobath, with areas of supercritical bathymetry along the shelf break rim reflecting a large fraction of the onshore-directed $\mathbf{EF}$ to deeper waters.

This study has helped us identify areas of intensified internal tide generation and propagation on the Oregon shelf, directing future observational and modeling studies toward better understanding the role of the tidal currents in the coastal ocean.
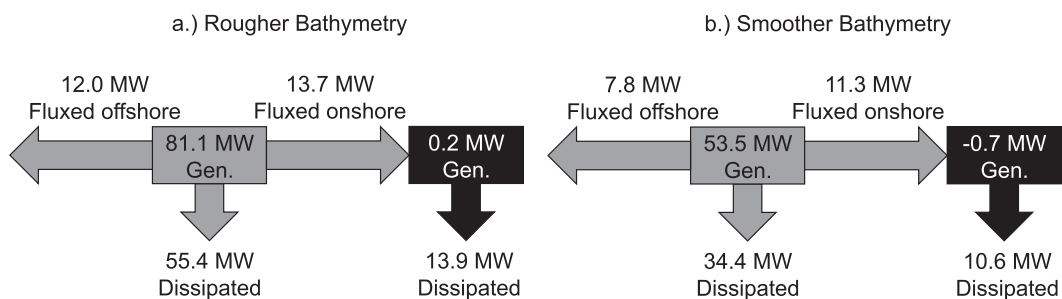
FIG. 25. Diagrams summarizing time-averaged TEC, dissipation, and $\mathbf{EF}$ over the slope (half-tone) and the shelf (black): (a) the rougher bathymetry case and (b) the smoother bathymetry case.

REFERENCES

Allen, J. S., P. A. Newberger, and J. Federiuk, 1995: Upwelling circulation on the Oregon continental shelf. Part I: Response to idealized forcing. *J. Phys. Oceanogr.,* **25,** 1843–1866.

Baines, P. G., 1982: On internal tide generation models. *Deep-Sea Res.,* **29,** 307–338.

Batchelder, H. P., and Coauthors, 2002: The GLOBEC Northeast Pacific California Current System program. *Oceanography,* **15,** 36–47.

Bennett, A. F., 1992: *Inverse Methods in Physical Oceanography.* Cambridge University Press, 346 pp.

Boyd, T., M. D. Levine, P. M. Kosro, S. R. Gard, and W. Waldorf, 2002: Observations from moorings on the Oregon continental shelf, May–August 2001. Oregon State University College of Oceanic and Atmospheric Sciences Data Rep. 190, 195 pp.

Chapman, D. C., 1985: Numerical treatment of cross-shelf open boundaries in a barotropic ocean model. *J. Phys. Oceanogr.,* **15,** 1060–1075.

Chavanne, C., P. Flament, D. Luther, and K.-W. Gurgel, 2010: The surface expression of semidiurnal internal tides near a strong source at Hawaii. Part II: Interactions with mesoscale currents. *J. Phys. Oceanogr.,* **40,** 1180–1200.

Chen, D., H. W. Ou, and C. Dong, 2003: A model study of internal tides in the coastal front zone. *J. Phys. Oceanogr.,* **33,** 170–187.

Egbert, G. D., and S. Y. Erofeeva, 2002: Efficient inverse modeling of barotropic ocean tides. *J. Atmos. Oceanic Technol.,* **19,** 183–204.

——, A. F. Bennett, and M. G. G. Foreman, 1994: TOPEX/ POSEIDON tides estimated using a global inverse model. *J. Geophys. Res.,* **99,** 24 821–24 852.

Erofeeva, S. Y., G. D. Egbert, and P. M. Kosro, 2003: Tidal currents on the central Oregon shelf: Models, data, and assimilation. *J. Geophys. Res.,* **108,** 3148, doi:10.1029/2002JC001615.

Fairall, C. W., E. F. Bradley, J. S. Godfrey, G. A. Wick, J. B. Edson, and G. S. Young, 1996a: Cool-skin and warm-layer effects on sea surface temperature. *J. Geophys. Res.,* **101,** 1295–1308.

——, ——, D. P. Rogers, J. B. Edson, and G. S. Young, 1996b: Bulk parameterization of air-sea fluxes for Tropical Ocean-Global Atmosphere Coupled-Ocean Atmosphere Response Experiment. *J. Geophys. Res.,* **101,** 3747–3764.

Federiuk, J., and J. S. Allen, 1995: Upwelling circulation on the Oregon continental shelf. Part II: Simulations and comparisons with observations. *J. Phys. Oceanogr.,* **25,** 1867–1889.

Flather, R. A., 1976: A tidal model of the north-west European continental shelf. *Mem. Soc. Roy. Sci. Liege,* **6,** 141–164.

Galperin, B., L. H. Kantha, S. Hassid, and A. Rosati, 1988: A quasi-equilibrium turbulent energy model for geophysical flows. *J. Atmos. Sci.,* **45,** 55–62.

Hall, P., and A. M. Davies, 2007: Internal tide modelling and the influence of wind effects. *Cont. Shelf Res.,* **27,** 1357–1377.

Hayes, S. P., and D. Halpern, 1976: Observations of internal waves and coastal upwelling on the Oregon coast. *J. Mar. Res.,* **34,** 247–267.

Hodur, R. M., 1997: The Naval Research Laboratory's Coupled Ocean/Atmosphere Mesoscale Prediction System (COAMPS). *Mon. Wea. Rev.,* **125,** 1414–1430.

Jachec, S. M., O. B. Fringer, R. L. Street, and G. Margot G, 2007: Effects of grid resolution on the simulation of internal tides. *Int. J. Offshore Polar Eng.,* **17,** 105–111.

Kalnay, E., and Coauthors, 1996: The NCEP/NCAR 40-Year Reanalysis Project. *Bull. Amer. Meteor. Soc.,* **77,** 437–471.

Kelly, S. M., and J. D. Nash, 2010: Internal-tide generation and destruction by shoaling internal tides. *Geophys. Res. Lett.,* **37,** L23611, doi:10.1029/2010GL045598.

Koch, A. O., A. L. Kurapov, and J. S. Allen, 2010: Near-surface dynamics of a separated jet in the coastal transition zone off Oregon. *J. Geophys. Res.,* **115,** C08020, doi:10.1029/ 2009JC005704.

Kosro, P. M., 2003: Enhanced southward flow over the Oregon shelf in 2002: A conduit for subarctic water. *Geophys. Res. Lett.,* **30,** 8023, doi:10.1029/2003GL017436.

Kundu, P. K., 1976: Ekman veering observed near the ocean bottom. *J. Phys. Oceanogr.,* **6,** 238–242.

Kurapov, A. L., G. D. Egbert, J. S. Allen, R. N. Miller, S. Y. Erofeeva, and P. M. Kosro, 2003: The M_2 internal tide off Oregon: Inferences from data assimilation. *J. Phys. Oceanogr.,* **33,** 1733–1757.

——, J. S. Allen, G. D. Egbert, and R. N. Miller, 2005: Modeling bottom mixed layer variability on the mid-Oregon shelf during summer upwelling. *J. Phys. Oceanogr.,* **35,** 1629–1649.

——, ——, and ——, 2010: Combined effects of wind-driven upwelling and internal tide on the continental shelf. *J. Phys. Oceanogr.,* **40,** 737–756.

Marchesiello, P., J. C. McWilliams, and A. Shchepetkin, 2001: Open boundary conditions for long-term integration of regional oceanic models. *Ocean Modell.,* **3,** 1–20.

Maturi, E., A. Harris, C. Merchant, J. Mittaz, B. Potash, W. Meng, and J. Sapper, 2008: NOAA's sea surface temperature products from operational geostationary satellites. *Bull. Amer. Meteor. Soc.,* **89,** 1877–1888.

Mellor, G. L., and T. Yamada, 1982: Development of a turbulence closure model for geophysical fluid problems. *Rev. Geophys. Space Phys.,* **20,** 851–875.

Mooers, C. N. K., 1970: The interaction of an internal tide with the frontal zone of a coastal upwelling region. Ph.D. thesis, Oregon State University, 480 pp.

——, 1975a: Several effects of a baroclinic current on the cross-stream propagation of inertial-internal waves. *Geophys. Astrophys. Fluid Dyn.,* **6,** 277–284.

——, 1975b: Several effects of a baroclinic currents on the three-dimensional propagation of inertial-internal waves. *Geophys. Astrophys. Fluid Dyn.,* **6,** 245–275.

NOAA, 1988: Digital relief of the surface of the earth: bathymetry/ topography data. National Geophysical Data Center Data Announcement 88-MGG-02.

Oke, P. R., and Coauthors, 2002a: A modeling study of the three-dimensional continental shelf circulation off Oregon. Part I: Model–data comparisons. *J. Phys. Oceanogr.,* **32,** 1360–1382.

——, J. S. Allen, R. N. Miller, and G. D. Egbert, 2002b: A modeling study of the three-dimensional continental shelf circulation off Oregon. Part II: Dynamical analysis. *J. Phys. Oceanogr.,* **32,** 1383–1403.

O'Keefe, S., 2005: Observing the coastal ocean with HF radar. M.S. thesis, Oregon State University, 103 pp.

Park, J.-H., and D. R. Watts, 2006: Internal tides in the southwestern Japan/East Sea. *J. Phys. Oceanogr.,* **36,** 22–34.

Pereira, A. F., B. M. Castro, L. Calado, and I. C. A. da Silveira, 2007: Numerical simulation of M_2 internal tides in the South Brazil Bight and their interaction with the Brazil Current. *J. Geophys. Res.,* **112,** C04009, doi:10.1029/2006JC003673.

Ramp, S. R., and F. L. Bahr, 2008: Seasonal evolution of the upwelling process south of Cape Blanco. *J. Phys. Oceanogr.,* **38,** 3–28.

Samelson, R., and Coauthors, 2002: Wind stress forcing of the Oregon coastal ocean during the 1999 upwelling season. *J. Geophys. Res.,* **107,** 3034, doi:10.1029/2001JC000900.

Shchepetkin, A. F., and J. C. McWilliams, 2005: The Regional Oceanic Modeling Systems (ROMS): A split-explicit, free-surface, topography-following-coordinate oceanic model. *Ocean Modell.,* **9,** 347–404, doi:10.1016/j.ocemod.2004.08.002.

Springer, S. R., R. M. Samelson, J. S. Allen, G. D. Egbert, A. L. Kurapov, R. N. Miller, and J. C. Kindle, 2009: A nested grid model of the Oregon Coastal Transition Zone: Simulations and comparisons with observations during the 2001 upwelling season. *J. Geophys. Res.,* **114,** C02010, doi:10.1029/2008JC004863.

Torgrimson, G. M., and B. M. Hickey, 1979: Barotropic and baroclinic tides over the continental slope and shelf off Oregon. *J. Phys. Oceanogr.,* **9,** 946–961.

Wunsch, C. H., 1975: Internal tides in the ocean. *Rev. Geophys. Space Phys.,* **13,** 167–182.

Xing, J., and A. M. Davies, 1997: The influence of wind effects upon internal tides in shelf edge regions. *J. Phys. Oceanogr.,* **27,** 2100–2125.

——, and ——, 1998: Influence of stratification upon diurnal tidal currents in shelf edge regions. *J. Phys. Oceanogr.,* **28,** 1803–1831.

——, and ——, 2005: Influence of a cold water bottom dome on internal wave trapping. *Geophys. Res. Lett.,* **32,** L03601, doi:10.1029/2004GL021833.